REGULAR ARTICLE

Natural hydrogen system evaluation in the São Francisco Basin (Brazil)

Vivian Azor de Freitas[1,2,*] , Alain Prinzhofer[3], João Batista Françolin[4], Francisco José Fonseca Ferreira[5], and Isabelle Moretti[6]

[1] Department of Chemistry, Life Science and Environmental Sustainability, University of Parma, Parco Area delle Scienze, 157/a, 43100 Parma, Italy
[2] National Agency of Petroleum, Natural Gas and Biofuels (ANP), Avenida Rio Branco 65, 20090-004 Rio de Janeiro, Brazil
[3] GEO4U, Centro Empresarial Mourisco, Praia de Botafogo 501, 20090-004 Rio de Janeiro, Brazil
[4] GEORISK, Rua Souza Lima 280, Copacabana, 22250-040 Rio de Janeiro, Brazil
[5] Federal University of Paraná, Department of Geology, Laboratory for Research in Applied Geophysics, Avenida Cel. Francisco H. dos Santos, 100, Jardim das Américas, 81530-000 Curitiba, PR, Brazil
[6] UPPA, LFCR, Rue de l'universitée, 64012, Pau, France

Abstract. The São Francisco Basin (SFB), a double foreland bordered by two Neoproterozoic belts, hosts a proven hydrogen (H_2) system, demonstrated by high concentrations in boreholes and numerous surface H_2 emissions, some long-term monitored. However, no detailed study has been conducted to correlate these H_2 occurrences with subsurface geological features. Therefore, this study evaluated the H_2 system components in the SFB, using public geophysical and well data previously acquired. The investigation revealed that wells drilled in structural traps contain natural gas and variable amounts of H_2, ranging from a few percent to 41%, at depths between 300 m and nearly 4 km, particularly within Neoproterozoic units. These intervals exhibit high neutron log readings when the H_2 concentration is higher than that of CH_4. The H_2-rich layers exhibit very low porosity and permeability and are overlapped by more impermeable zones within the same lithostratigraphic units. The low density of sub-circular depressions (SCD) near most H_2-bearing wells could be due to effective seal, however, the type of soil is likely to strongly influence the SCD formation since our investigation revealed that SCDs are predominantly found in poorly compacted sediments of the Cenozoic cover of the SFB. Potential H_2-generating rocks include the Archean and Paleoproterozoic Banded Iron Formation (BIF), Neoproterozoic BIFs and ultramafic bodies, Cretaceous ultramafic intrusions, and the overmature organic-rich source rocks. A complementary influence of radiolysis cannot be ruled out. Significant magnetic anomalies, as indirect indicators of ferrous bodies, suggest potential H_2 kitchens. Notably, the Pirapora Anomaly, in the central part of the basin, may reveal the presence of iron-rich bodies at great depth. However, most of the H_2-bearing wells are not in their zone of influence, suggesting the presence of other H_2 kitchens, such as those indicated by the magnetic anomalies beneath the Alto do Paranaíba Igneous Province (APIP) and Quadrilátero Ferrífero (QF), extending to the internal part of the basin. The multiphase structural history of the SFB may allow gas migration in different ways. The relative influence of long-distance migration, usually from the compressive front toward the foreland part of the basin, and a vertical short-distance migration from magmatic intrusion can be highlighted. Additionally, denudation accelerated by the opening of the Atlantic Ocean may play a role in the H_2 flow measured in this basin.

Keywords: Natural hydrogen, São Francisco Basin, BIF, Pirapora magnetic anomaly.

* Corresponding author: vivian.azordefreitas@unipr.it; vafreitas@anp.gov.br

1 Introduction

1.1 Natural hydrogen

Diversification of the energy matrix, focusing on clean and cost-effective options is increasingly pursued worldwide. In this context, dihydrogen (H_2) may play a key role in decarbonizing the industry, and H_2 from geological (or natural) sources is targeted to supplement manufactured H_2. Due to its low carbon emissions and wide range of uses in the industrial, transportation and energy sectors, H_2, which was up to now mainly a raw material for chemical applications, stands also out as an alternative source of energy.

Among the H_2 types, natural H_2 has an excellent Life Cycle Analysis, it could be cleaner than manufactured H_2 (Brandt, 2023) and might also be economically advantageous, since it is naturally generated in subsurface without the use of additional energy sources.

Natural H_2 is generated by different subsurface processes, such as hydrothermal alteration of iron-rich rocks, water radiolysis by natural radioactive decay of U, Th and K, biological activities, mechanoradical, magma degassing and decomposition of organic matter (Klein *et al.*, 2020; Lévy *et al.*, 2023; Zgonnik, 2020). In terms of significance, oxido-reduction, radiolysis and late maturation of the organic matter are considered as the main processes. Kinetics of these different processes may vary from very slow for the radioactivity (*e.g.*, half-life for uranium-235 = 700 Ma) to almost immediate for the oxido-reduction at the optimum temperature (H_2 is generated within four months at 80 °C from magnetite, Geymond *et al.*, 2023). As a result, the generation rate varies and is sometimes short at the human scale. The retention time of H_2 in the reservoirs could also be variable. In some cases, H_2 appears to have a residence time underground a thousand times shorter than hydrocarbons (HC, Prinzhofer and Cacas-Stentz, 2023). However, below salt layers as in the Amadeus Basin in Australia, it can be retained for hundred million years (Leila *et al.*, 2022). Reservoirs sealed by caprocks are usually targeted on H_2 exploration. In Mali, at Bourakebougou, the only place where the H_2 has been exploited so far, carbonate reservoirs are covered by dolerite sills and sandstones by shale. (Maiga *et al.*, 2023a,b). Additionally, targeting H_2 flows in the subsurface can also be considered an exploration option.

Following positive results achieved by pioneering studies focusing on natural hydrogen exploration (Guélard *et al.*, 2017; Prinzhofer *et al.*, 2018; Prinzhofer *et al.*, 2019; Zgonnik *et al.*, 2015) and more than 10 years of successful H_2 production in Mali, the scientific community and industry began to look at the matter with more careful eyes. This was reflected in the remarkable increase in publications related to the topic and the emergence of companies dedicated to the natural H_2 exploration in the last few years.

In this scenario of searching for H_2, intracratonic basins have favorable conditions for H_2 occurrences, especially due to the presence of rocks rich in iron and radioactive elements. A main proxy for surface H_2 exploration in these geological domains is the SCDs recognized by satellite images, also called fairy circles. They were been first described by Larin *et al.* (2015) in Russia and then used worldwide to track prospective areas for natural hydrogen (Lévy *et al.*, 2023; Moretti *et al.*, 2021a; Zgonnik *et al.*, 2015). Significant amounts of H_2 were detected inside the soil of the SCDs in several cratons worldwide, such as in Brazil, the United States, Australia, Namibia and Russia (Frery *et al.*, 2021; Larin *et al.*, 2015; Moretti *et al.*, 2021a, 2022). The origin of these features is still unclear. Donze *et al.* (2020) relate the SCD of the São Francisco Basin (SFB) to the process of carbonate dissolution and sinkhole formation, while Moretti *et al.* (2021b) associate these vegetation changes with the soil characteristics and microorganism in case of gas escape. Infrared satellite images allow to better define these SCDs than the Google Earth approach (Lévy *et al.*, 2023).

1.2 Evidence of H_2 presence and leakage in the São Francisco Basin.

The SFB, Figure 1, is rather well-known in terms of natural H_2 since it has been studied for over 6 years. Numerous H_2 surface emanations have been recorded, and previous wells, which will be discussed later, have reported high concentrations of H_2. Reis and Fonseca (2021) reported concentrations of up to 40% of H_2 in HC wells associated with remarkable amounts of helium. However, no wells specifically targeting H_2 reservoirs have been drilled, because the current Brazilian regulation concerning natural hydrogen exploration is still in the process of being implemented, but the expectations are high if there is no doubt that the hydrogen system is proven in the SFB. Nonetheless, questions about active H_2-generating rocks, underground reservoirs, traps, seals, and types of fluid are still open.

Several SCDs have been tested positively for H_2 in the SFB. Long-term monitoring at two of these sites detected large H_2 pulses (over 10,000 ppm) and H_2 flux of 0.03–0.04 $m^3/m^{-2}/day^{-1}$ that was extrapolated to about 700 kg of H_2/day (Moretti *et al.*, 2021a; Prinzhofer *et al.*, 2019). Soils have been also studied and the microorganisms that consume part of the H_2 are characterized (Myagkiy *et al.*, 2019, 2020).

Flude *et al.* (2019) also noticed the presence of helium with a crustal signature. Donze *et al.* (2020) highlight the U, K and Th content of the basement in the SFB that may favor radiolysis as the main process for H_2 generation. Moretti *et al.* (2021a,b) proposed the Archean/Paleoproterozoic iron-rich facies as the principal generating rocks and Donze *et al.* (2020) favored the deep magnetic anomaly near the studied fairy circles, considering radiolysis and oxidation of ultramafic rocks as potential H_2 source. The role of sedimentary rocks such as the Banded Iron Formation (BIF), not yet really quantified in 2020, was not considered. Notably, none of these authors studied the rocks and their iron content. The Archean BIF has been studied by Geymond *et al.* (2022) in Australia, showing that BIF could be a good generating rock for H_2 at rather low temperatures. Moretti *et al.* (2022) and Roche *et al.* (2024) studied the Neoproterozoic BIF in Namibia and also concluded its high potential for H_2 generation.

This study aims to evaluate the elements of the H_2 system in the central and southern SFB using a substantial number of seismic, magnetic and well data provided by
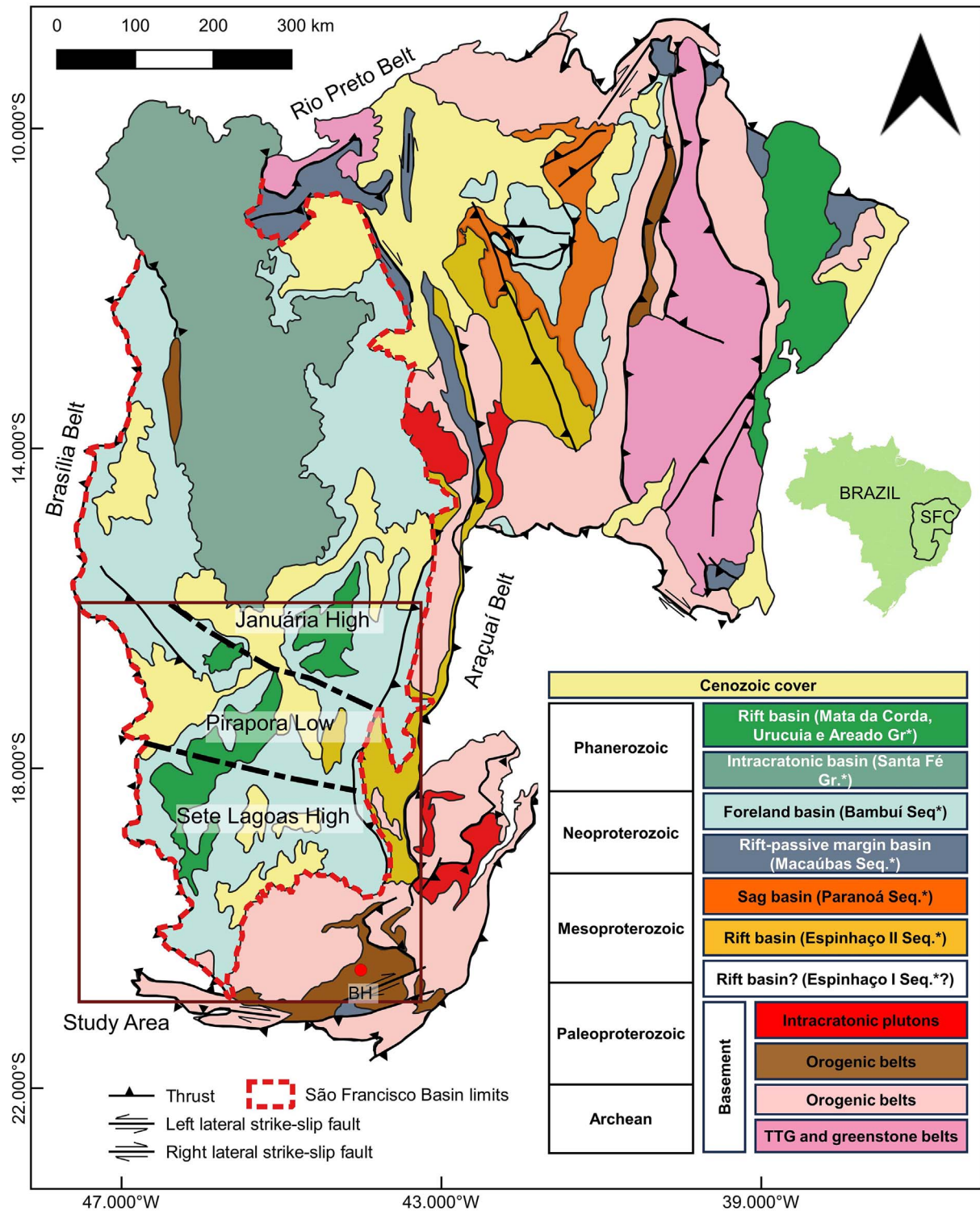
Fig. 1. Simplified geological map of São Francisco Craton (SFC), outlining the São Francisco Basin and its stratigraphic chart, based on Delgado *et al.* (2003), Reis and Alkmim (2015), Garayp and Frimmel (2022). The Januária High, Pirapora Low and Sete Lagoas High are based on Reis *et al.* (2017). *Sequence and group names for the area within the São Francisco Basin. BH = Belo Horizonte City.

Brazilian government institutions. After a summary of the geological setting of the SFB, we will list and map the H_2 potential generation zones. Well data will be incorporated focusing on the gas found during drilling or in the tested reservoirs. Geophysical data allows us to propose traps and highlight the magnetic anomalies. Finally, we will discuss possible migration pathways between the proposed kitchens and the known accumulations and emanations.
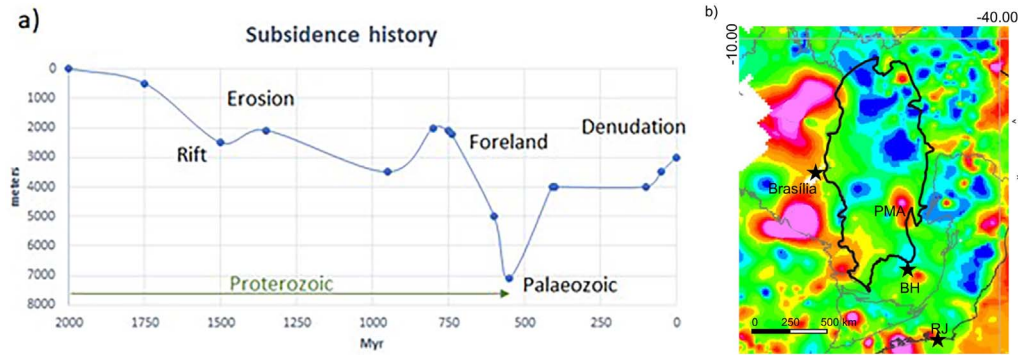
Fig. 2. Basin subsidence and thermal state. a) schematic global subsidence curve of the SFB based on sedimentary hiatuses and amount of erosion. b) current heat flow on the SFB, modified from Guimarães *et al.* (2022). PMA corresponds to Pirapora Magnetic Anomaly, BH to Belo Horizonte city and RJ to Rio de Janeiro city.

The methods used in this study are presented in the Appendix, including the issues faced with the geochemical database, which required a strict quality control.

2 The São Francisco Basin

2.1 Geological setting

Located in the South American Platform, over five Brazilian States, the São Francisco Craton (SFC, Fig. 1) hosts rock sequences from Paleoarchean to the Cenozoic and corresponds to the Brazilian counterpart of Congo Craton in Africa. Seismic and gravimetric data indicate a constant crustal thickness of 40 km (±1 km) all over the studied area (Assumpção *et al.*, 2017).

The São Francisco basin corresponds to one of the main tectonic components of the São Francisco craton, covering its southern NS-trending lobe (Alkmim and Martins-Neto, 2001; Martins-Neto, 2009; Reis *et al.*, 2017).

The SFB hosts sedimentary rocks ranging from Paleoproterozoic (about 1.8 Ga) to Mesozoic in age, which unconformably overlie Archean and Paleoproterozoic basement assemblages. The basin records various extensional phases, some of them followed by a thermal subsidence phase that took place between the late Paleoproterozoic and Neoproterozoic and resulted in the deposition of Espinhaço Supergroup, the Paranoá group and the Jequitaí Formation and correlatives. Erosional phases separate the subsidence periods and result in hiatus and unconformities clearly visible on seismic lines. The deposition of the Bambuí Group took place when the São Francisco paleocontinent was converted into a foreland basin system, during the Neoproterozoic/early Paleozoic orogenies leading to the West Gondwana assembly (Alkmim and Martins-Neto, 2001; Reis *et al.*, 2017).

The Proterozoic to early Paleozoic strata in the basin may reach more than 10 km in thickness and they are covered by thin Phanerozoic units comprising the Santa Fé (Permo-Carboniferous), Areado, Mata da Corda, and Urucuia groups (Cretaceous) (Alkmim and Martins-Neto, 2001; Zalán and Silva, 2007).

Three main tectonic events were recognized using seismic interpretation, well and aerogravimetric and aeromagnetometric data (Reis and Alkmim, 2015) and they are depicted on a synthetic subsidence curve in Figure 2a. This sketch of the burial history is simplified to help visualize the major phases of burial and erosion in this basin. The age of erosion is deduced from sedimentary hiatuses. The amount of erosion was inferred from the seismic data (southwestern part of the basin).

The first tectonic event corresponds to Proterozoic rifting episodes that culminated in the nucleation and successive reactivations of the NW-SE oriented Pirapora aulacogen. The graben is the most prominent basement structure of the basin and is bounded by Sete Lagoas High, to the south, and Januária High, to the north. At least two different rifting phases, generating two sequences separated by a regional unconformity, can be recognized in the basin.

During the Late Neoproterozoic/Early Paleozoic West Gondwana Amalgamation, the São Francisco lithosphere experienced a deep burial and two diachronic foreland fold-thrust belts were formed: the thin-skinned Brasília to the west and the thin-to-thick-skinned Araçuaí to the east (Reis and Alkmim, 2015). The amplitude of uplift since 600 Ma and its rate increased since the opening of the Atlantic. They were extrapolated from the AFTA (Apatite Fission-Track Analysis) data published for southeastern Brazil (Hackspacher *et al.*, 2004) and they indicate an increase of uplift during the last 65 Ma.

The last event is Cretaceous in age, it took place during the South Atlantic Ocean opening and led locally to the deposition of the Phanerozoic deposits, as well as the emplacement of alkaline intrusions and NW-SE dyke swarms.

2.2 Basement and H₂ potential generating rocks

The basement rocks of the SFB are composed of Paleoproterozoic and Archean rocks older than 1.8 Ga (Alkmim and Martins-Neto, 2001). These units include Archean TTG (Tonalite–Trondhjemite–Granodiorite) complexes, greenstone belts successions, metavolcanic rocks, K-rich granitoids, BIFs and Paleoproterozoic igneous and metasedimentary rocks (Teixeira *et al.*, 2017).

Many rocks may be candidates for H₂ generation, such as (1) Archean greenstone belts, containing ultramafic rocks sequences, (2) the BIFs from both Archean/Paleoproterozoic

(to the southeast) and from Neoproterozoic (east) and (3) Archean TTG complexes and K-rich granitic plutons, rich in radioactive elements. Most of these units outcrop outside the basin boundaries, especially in its southern and western portions (Fig. 1).

The world-class metallogenetic province named Quadrilátero Ferrífero (QF), is located to the south of the basin and hosts several iron and gold mines. The most impressive iron-rich rocks correspond to Paleoproterozoic BIFs with iron content of around 50% (Vale Annual Report, 2023), which can be pointed as potential H_2 source (Geymond et al., 2022; Moretti et al., 2021a). Additionally, in the eastern side of the basin, in the Araçuaí Belt, outcrops of the Ribeirão da Folha Formation, containing Neoproterozoic BIF (Amaral et al., 2020).

Indirect ferrous rock indicators are shown by geophysical data in the central part of the basin, where a very large and isolated magnetic anomaly known as the Pirapora magnetic anomaly has been identified (Borges and Drews, 2001). These authors assume that the anomaly corresponds to a body located more than 5000 meters deep, which can match with a large magnetic mineral-rich feature located in the basement level.

Apart from the basement rocks, it is noteworthy the presence of ultramafic rocks comprising the Cretaceous Alto do Paranaíba Igneous Province (APIP), one of the largest mafic potassic provinces in the world (Gibson et al., 1995). In the southwestern portion of basin, the APIP expression occurs as circular plutonic complexes: Araxá, Salitre, Serra Negra, and Tapira, that encompass carbonatite, peridotite, pyroxenite and dunite bodies (Gibson et al., 1995). The Kimberlite pipes carried up peridotites from the mantle and sampled the mantle root of the SFC (Fernandes et al., 2021). These authors studied 31 mantle xenoliths from the Cretaceous kimberlites intruding the Brasília Belt in the APIP province and their study highlighted the high olivine content (83%), supplemented with 12% of orthopyroxene and 5% of clinopyroxene. The same authors state that some of the olivine crystals are richer in Fe (Mg# < 90), compared to other cratonic areas (Mg# between 90 and 93). Their volume and structural position have also to be considered before taking them into account as possible generating rocks for the H_2 found in the western part of the basin.

In addition, lavas and tuffs of the Mata da Corda Formation represent the surface expression of APIP and correspond to (ultra) mafic potassic rocks containing essentially clinopyroxenes, perovskite, magnetite and occasionally olivine, phlogopite, melilite pseudomorphs and apatite (Gibson et al., 1995; Sgarbi and Valenca, 1995).

The recent tectonic history in the SFB is mainly resumed in uplift and erosion, as showed in Figure 2a (Fonseca et al., 2021; Tribaldos et al., 2017). As a result, an increase of temperature cannot be postulated to generate H_2 (neither methane) for the last 500 Ma. Concerning the hydrocarbons, it means that only very old accumulations could be expected. Concerning H_2, at the opposite, rocks that were at a too high temperature to generate H_2 may reach the right temperature window due to this Mesozoic and Tertiary denudation phase.

2.3 Heat flow

The geothermal gradient measured in the wells varies from rather low in the south and western part around 19 ± 2 °C/km to values between 24 and 34 °C/km in the northeast part (wells PTRA-5, 7 and 9). This non-homogeneity has been also noticed by Guimarães et al., (2022), in their mapping of terrestrial heat flow in Brazil. Values in the SFB vary from a low 40 mW/m² to a locally rather high 90 mW/m². The higher values are, however, limited to a small zone around 17°30′S and 45°W that corresponds also to the Pirapora magnetic anomaly (Fig. 2b). The remaining part could be considered relatively cold. Since the thermal conductivity of iron and other metals is much higher than that of carbonates or quartz (80 Wm^{-1} K^{-1} for iron, 2 to 3 Wm^{-1} K^{-1} for a sandstone) an influence of highly metalliferous rocks on the calculated heat flux map cannot be ruled out. The anomalies do not correspond to deep-seated or tectonic phenomena and are more likely to be gradient anomalies than heat flow anomalies, in this case well data is more reliable.

2.4 Reservoir units

Intervals containing natural gas have been found in the Proterozoic sequence of the SFB. Facies include sandstones from Paranoá-Espinhaço and Macaúbas sequences, and carbonates and siliciclastic rocks from Bambuí Sequence (Dignart, 2013; Reis, 2018). In general, they show very low porosity and permeability and are considered tight reservoirs. However, locally, the Paranoá-Espinhaço Sequence which encompasses sandstones, arkosic sandstones and coarse-grained sandstones shows secondary porosity up to 10% due to cement and minerals dissolution (Reis, 2018). Carbonate rocks of the Bambuí Sequence correspond to calcarenite, calcirudite, calcilutite and dolomite from the Sete Lagoas Formation with vugular or intracrystalline secondary porosity. For these facies, locally in the upper part of the formation, this secondary porosity may reach up to 6–8% (Reis, 2018).

Siliciclastic rocks of the Bambuí Sequence consist of interbedded siltstones, mudstones, and fine sandstones, with a maximum secondary porosity of 1–2% related to fractures (Reis, 2018).

2.5 Fluids from well data

A total of 41 exploratory wells were drilled in the SFB between 1988 and 2013, aimed at HC exploration. Among the wells, evidence of HC, especially natural gas, was detected in 29 of them, of which eight have also some H_2 content, all of them drilled within the study area from 2011 and 2012. The others were dry, and liquid petroleum was never found.

2.5.1 Gas composition and isotopic analyses

Compositional gas analyses are available for 15 wells (Table Compositional and isotopic available data, supplementary data), including the eight wells with variable amounts of H_2: PTRA-1, PTRA-2, PTRA-5, PTRA-6,

PTRA-10, PTRA-12, PTRA-13, and PTRA-14. The analyses were performed by Isotech laboratories Inc/Wetherford Laboratories Brazil, contracted by PETRA, the oil company that drilled the wells.

The original dataset of 334 gas composition analyses from the 15 wells underwent a quality control and air correction, better described in Appendix, resulting in a reduced dataset of 14 reliable cylinder samples from only four wells (PTRA-1, PTRA-2, PTRA-5 and PTRA-14). The geochemical assessment focused on the compositional and isotopic analysis of these samples, presented in Table 1. Considering the questionable ability of isotube and isojar analyses to demonstrate the real quantities of gas in the subsurface, they were not used for quantitative characterization of the gas. However, these analyses can qualitatively indicate the presence of gas that does not originate from atmospheric contamination, such as H_2 and methane. Thus, wells PTRA-6, PTRA-10, PTRA-12, and PTRA-13 containing only isotube and/or isojar samples can be considered H_2 hosted, even if it is hard to specify its quantity.

2.6 Well logs

Four wells with H_2 were submitted for a detailed investigation using well log and rock data: PTRA-1, PTRA-5, PTRA-12, and PTRA-13. The main purpose of the investigation was to identify the rock and fluid properties in the H_2-rich zones, looking for log patterns and similarities between wells and zones. The study was based on the Gamma Ray (GR), resistivity (deep), sonic, density, and neutron curves, and lithostratigraphic well tops (Fig. 3), using the software Petrel, version 2020.5 made by Schlumberger. Caliper curves were used as support to check the stability of the well.

Information from lithostratigraphic well tops, drill cuttings, sidewall and conventional cores descriptions were also used to describe the H_2 reservoirs.

2.7 TOC and pyrolysis

Total Organic Carbon (TOC) and pyrolysis data are available for 30 samples of drill cuttings and conventional cores from four wells, 1-BRSA-871-MG, 1-BRSA-948-MG, PTRA-14, and 1-RF-1 -MG. The predominant lithotype of the samples corresponds to shale, but siltstone, calcilutite and dolomite are also included in the dataset. A Neoproterozoic source rock is known in the west (well 9-PSB-9), and outcrops in the Brasília Belt, but has never been confirmed eastward.

In the SFC, fine-grained siliciclastic rocks from the Paranoá Sequence have a high TOC, of 3-4% on average and a maximum value of 15.6% (Martins-Neto, 2009). Shale and carbonate rocks of the Bambuí Sequence have TOC of up to 3.5% (Reis and Alkmim, 2015). The thickness of the Source Rock (SR) may be large, more than 600 m in the 9-PSB-009-MG well. Reis (2018) suggested that this SR has a high degree of thermal maturity and is overmature. The maximum of maturity was reached about 600 Ma ago. Postmature rocks rich in organic matter can also act as H_2 generating rock (Boreham *et al.*, 2023; Horsfield *et al.*, 2022; Moretti *et al.*, 2024).

3 Results

3.1 Surface features recognition

Around 1900 SCDs were mapped (Fig. 4) based on satellite images using manual mapping and including the ones already published by Moretti *et al.* (2021b) that correspond to a small central zone. Their sizes vary from a few tens of meters to 1.1 km in diameter. They are concentrated in the northern and western parts of the study area, mostly in thrust belt, lineaments and over ferruginous lateritic covers formed in the Cenozoic Era. Despite corresponding to around 70% of the study area, Archean and Proterozoic rock outcropping zones are not likely to hold these features.

In general, these features do not show a main preferred direction, presenting a roughly rounded shape. An exception is the southern part of the Cabeceiras Fault system, where the SCDs have a NW elongated shape, parallel to the terrain lineaments (in detail in Fig. 4).

Some areas with high SCD density were previously tested positive for H_2 emanation on surface (Moretti *et al.*, 2021a), especially in areas prone to fluid leakage.

3.2 Geophysical Interpretation

Regional interpretation of 2D seismic sections shows the relationship between the sedimentary sequences present in the SFB (Figs. 5a and 5b). The lower and upper Espinhaço sequences are separated by a well-defined unconformity and located within fault-bordered grabens (orange lines Fig. 5). Mesoproterozoic volcanic intrusions profusely intrude these lower and upper Espinhaço sequences, forming dikes and sills, which were folded and faulted during the Ediacaran orogeny (Fig. 5a).

The Januária High acts as the northern limit for the deposition of the sequences (Fig. 5b). The Macaúbas Sequence surpasses the rift limit and advances over the Januária High as a tabular and continuous package, with smooth variations in thickness. The Bambuí Sequence covers the entire set as a more homogeneous and slightly deformed package.

The top of the Archean/Paleoproterozoic basement, mapped based on seismic interpretation, occurs at a depth range from 0 s to around 4 s. The structural map shows an elongated NW-SE low and two highs. They correspond to the Pirapora Low, Januária High in the northwestern and Sete Lagoas High, in the southern part of the study area (Fig. 4).

The wells have been classically drilled targeting structural 3D closure traps (Fig. 6) and are mainly located in anticlines related to the two thrust belts that border the basin eastward and westward. One may notice that the wells located in the central part of this double foreland are without H_2 (blue dots Fig. 4) when all the ones with H_2 are closer from the borders (red dots Fig. 4).

3.3 Magnetic anomalies

The Total Field Magnetic Anomaly (TFA) map (Fig. 7) shows dipolar magnetic anomalies with normal and reversal

Table 1. Air-corrected gas compositional and isotopic analysis from cylinders previously collected during the well tests in the São Francisco Basin. The original data was in mol. % and ppm, after the air correction, they were normalized to 100%. Isotopic composition of H_2 is relative to VSMOW. Isotopic composition of carbon is relative to VPDB. nd= not detected, na= not analyzed, na*= Ar was measured as $Ar+O_2$%, and the value was used to the air correction. **Air contamination calculate based on the sum of O_2 and atmospheric N_2. Same well and depth samples correspond to different samples collected at the same depth interval and analyzed at different times.

Well name	PTRA-1	PTRA-1	PTRA-2	PTRA-2	PTRA-2	PTRA-2	PTRA-5	PTRA-5	PTRA-5	PTRA-5	PTRA-14	PTRA-14	PTRA-14	PTRA-14
Depth (m)	860–912	860–912	1790–1930	1790–1930	1790–1930	1790–1930	351–509	351–509	351–509	351–509	1779–1929	1779–1929	1779–1929	1779–1929
He %	0.96	0.98	na	na	1.15	1.57	1.00	na	0.61	na	0.61	0.61	0.62	0.59
H2%	40.4	41.1	nd	nd	0.07	1.04	25.1	25.3	32.8	31.0	0.19	0.18	0.19	0.23
A r %	0.07	0.09	na*	na*	0.79	0.30	0.05	na*	0.02	na*	0.17	0.47	0.20	0.13
CO2%	0.04	0.01	0.01	0.11	0.04	0.01	nd	0.01	0.01	0.02	0.15	0.08	0.09	0.01
N2%	15.7	16.4	37.0	36.5	35.1	36.5	6.21	5.86	2.13	1.74	9.83	9.97	9.83	9.27
CO %	nd	nd	nd	nd	nd	nd	nd	nd	nd	nd	nd	nd	nd	nd
C1%	39.3	38.2	59.3	59.6	58.8	56.7	66.4	67.7	63.5	65.5	87.7	87.4	87.7	88.4
C2%	2.76	2.69	3.12	3.15	3.38	3.19	1.15	1.10	0.91	0.88	1.28	1.29	1.29	1.27
C2H4%	nd	nd	0.00	0.00	nd	nd	nd	nd	nd	nd	nd	nd	nd	nd
C3%	0.32	0.31	0.42	0.43	0.48	0.45	0.05	0.05	0.04	0.04	0.04	0.04	0.04	0.04
C3H6%	nd	nd	nd	nd	nd	nd	nd	nd	nd	nd	nd	nd	nd	nd
iC4%	0.03	0.03	0.04	0.04	0.05	0.05	0.00	0.00	0.00	0.00	0.00	0.00	0.00	0.00
nC4%	0.05	0.05	0.06	0.07	0.08	0.08	0.00	0.00	0.00	0.00	0.00	0.00	0.00	0.00
iC5%	0.01	0.01	0.02	0.02	0.03	0.03	0.00	0.00	0.00	0.00	0.00	0.00	0.00	0.00
nC5%	0.34	0.01	0.01	0.01	0.01	0.01	0.00	0.00	0.00	0.00	0.00	0.00	0.00	0.00
C6+ %	0.07	0.01	0.01	0.01	0.02	0.04	0.01	0.00	0.00	0.00	0.00	0.00	0.00	0.00
Air Cor. % **	3.12	4.78	10.8	60.9	37.6	8.14	0.00	0.96	0.00	1.51	8.51	29.5	11.3	5.68
$\delta^{13}C1‰$	−26.3	−26.3	−48.5	−44.5	−48.1	−48.8	−44.7	−45.7	−51	−52.2	−46.9	−46.6	−46.6	−46
$\delta^{13}C2‰$	−29.7	−29.6	−42.5	−41.5	−42.1	−41.9	−31.6	−31.9	−28.5	−28.6	−42.4	−42.4	−42.4	−42.1
$\delta^{13}C3‰$	na	na	−39.6	−39.3	−39.5	−39.4	na	−27.9	na	−24.9	na	na	na	na
$\delta^{13}iC4‰$	na	na	na	na	−43.9	−43.8	na	na	na	na	na	na	na	na
$\delta^{13}nC4‰$	na	na	na	na	−40.2	−40	na	na	na	na	na	na	na	na
$\delta DC1‰$	−394	−397	−417	−407	−409	−414	−374	−369	−408	−404	−442	−442	−440	−443
$\delta DC2‰$	−294	−295	−274	−278	−271	−268	−281	−267	−301	−276	−331	−334	−332	−339
$\delta DC3‰$	na	na	na	na	−207	−210	na	na	na	na	na	na	na	na
$\delta DH2‰$	−707	−706	na	na	na	na	−736	na	−734	na	na	na	na	na
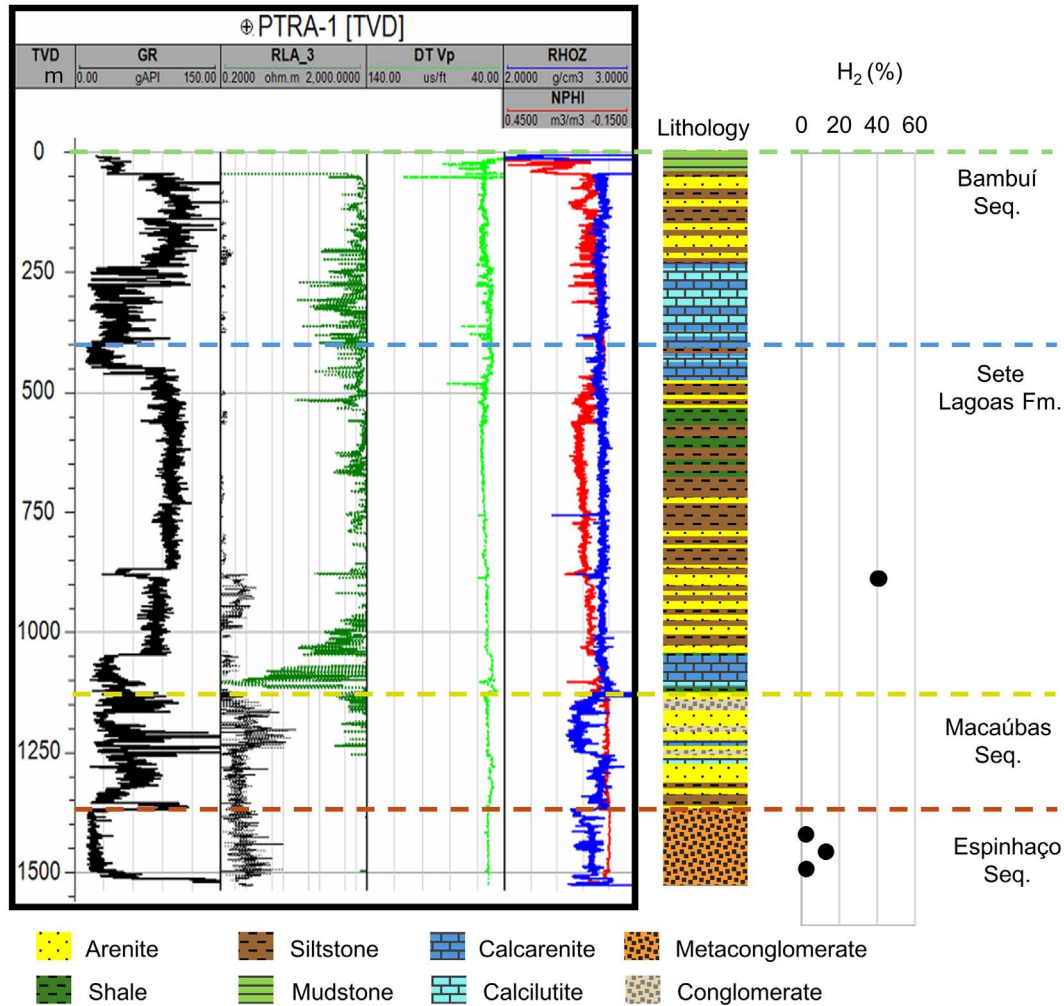
Fig. 3. Stratigraphic column, log and H_2 content in % from the well PTRA-1. H_2 amounts are derived from five samples. Two of these samples are listed in Table 1, obtained during the well test (860 to 912 m depth), with the reference depth (886 m) representing an average of the depth interval. They appear superimposed in the figure due to being from the same depth interval and exhibiting similar H_2 values. The remaining three samples correspond to isojar samples collected from 1419, 1455, and 1491 m depth; therefore, the accuracy of their value is questionable as discussed in item 3 of the Appendix. However, after air correction, these values are included in the graph to indicate that the Espinhaço Sequence also holds H_2 shows. GR corresponds to gamma ray, RLA_3 to resistivity, DT Vp to sonic, RHOZ to density and NPHI to neutron log.

magnetizations. These magnetic anomalies are better delimited in the Analytic Signal Amplitude (ASA) and Vertical Integral of the Analytic Signal (VIAS) maps, and they may indicate possible locations of ultrabasic-alkaline intrusions (Figs. 8a and 8b). The anomalies shown in VIAS may correspond to the deeper signals of the iron-rich bodies, as this method highlights the response of deep terrains, while high amplitudes of ASA show the magnetic response of the shallow basement or deep bodies with high magnetization.

Three main magnetic anomalies were recognized in the study area: (1) Alto do Paranaíba Mafic Alkaline Igneous Province (APIP) circular anomalies and Mata da Corda Formation outcrop; (2) Quadrilátero Ferrífero magnetic anomalies; and (3) Pirapora anomaly. Additionally, the ASA map (Fig. 8a) reveals smaller magnetic anomalies in the north (Januária High) and in the central-south area,

between the Pirapora anomaly and APIP. Those anomalies are absent or less evident in VIAS (Fig. 8b), which may correspond to shallower bodies of uncertain origin.

The circular and dipolar anomalies correspond mostly to pipe-type intrusive bodies, such as the Pirapora anomaly and the ones present in APIP. On the other hand, some anomalies non-dipolar may represent iron-rich rocks such as those from the Quadrilátero Ferrífero and from the Mata da Corda Formation.

The APIP magnetic anomalies stand out in the southwest area as dipolar anomalies in TFA and as high-amplitude circular anomalies of the ASA (Fig. 8a) and VIAS (Fig. 8b). They may correspond to the subsurface continuation of ultrabasic alkaline intrusions observed at the surface. In the southwest area, Mata da Corda Formation anomalies are coincident with most of its outcropping area, where probably its mafic layers are abundant.
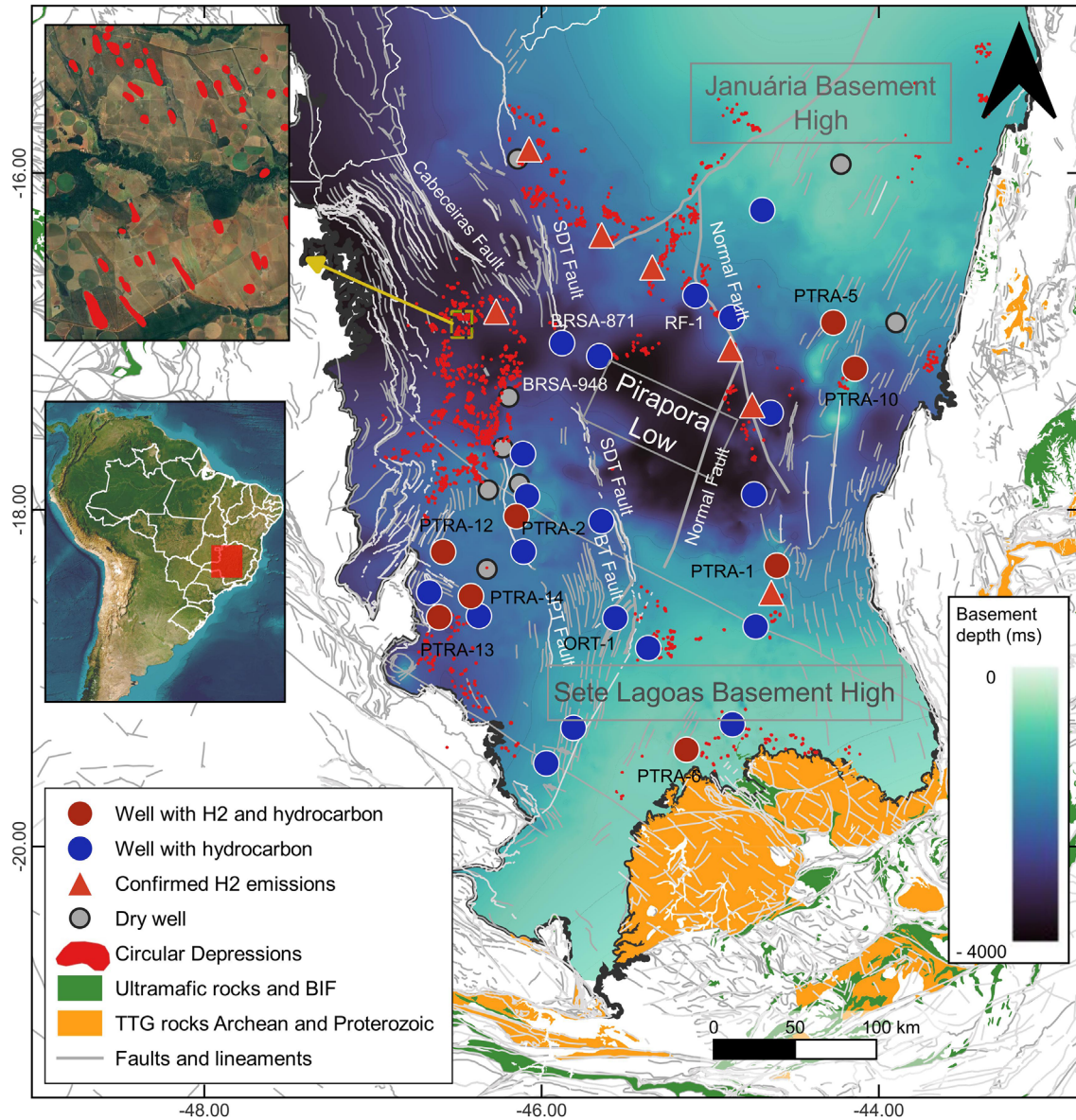
Fig. 4. Map of the central and southern portion of SFB (Minas Gerais State, Brazil), representing the area of interest of this work. The basement structural map was based on time-migrated seismic reflection surveys (TWT). Wells with H₂, SCDs and confirmed emissions of H₂ by Moretti *et al.* (2021a) and Geymond *et al.* (2022) are plotted over the basement structural map. Faults and lineaments from Geological Map scale 1:1,000,000 of Geological Survey of Brazil. SDT Fault = São Domingos Thrust Fault, BT Fault = Borrachudo Thrust Fault, JPT Fault = João Pinheiro Thrust Fault after Reis and Alkmim (2015).

In the south-east part of TFA, ASA, and VIAS maps, the QF is clearly abnormal. In this region, numerous iron mines and outcrops of iron-rich sequences (Figs. 7 and 8) present positive anomalies as a result of the iron-rich rocks occurrences (BIFs and ultramafic bodies) in the surface and deep underground.

The Pirapora magnetic anomaly is remarkable, both in intensity and in size, it is located in the northern border of the Pirapora Low, where the lower Espinhaço Sequence is thick. This anomaly is an inverted polarity dipole that ranges from 227 to −948, nT, with an aerial extent of approximately 80 × 60 km in map view (Figs. 7, 8a, 8b).

The potential Pirapora anomaly depth was estimated using 3D Euler deconvolution based on TFA and VIAS grids. According to calculations, the central part of the anomaly is located very deep between 22 and 44 km deep, considering the TFA grid, and 33 to over 44 km for the VIAS grid. These depths are clearly too large since the Curie temperature is not so deep, 741 °C for the iron. Considering the gradient of 25 °C/km and 20 °C as the average surface temperature, at 30 km the temperature reaches 770 °C. With a gradient of 20 °C/km, 740 °C will be reached at a depth of 36 km. No magnetic signal is expected to come from a larger depth.
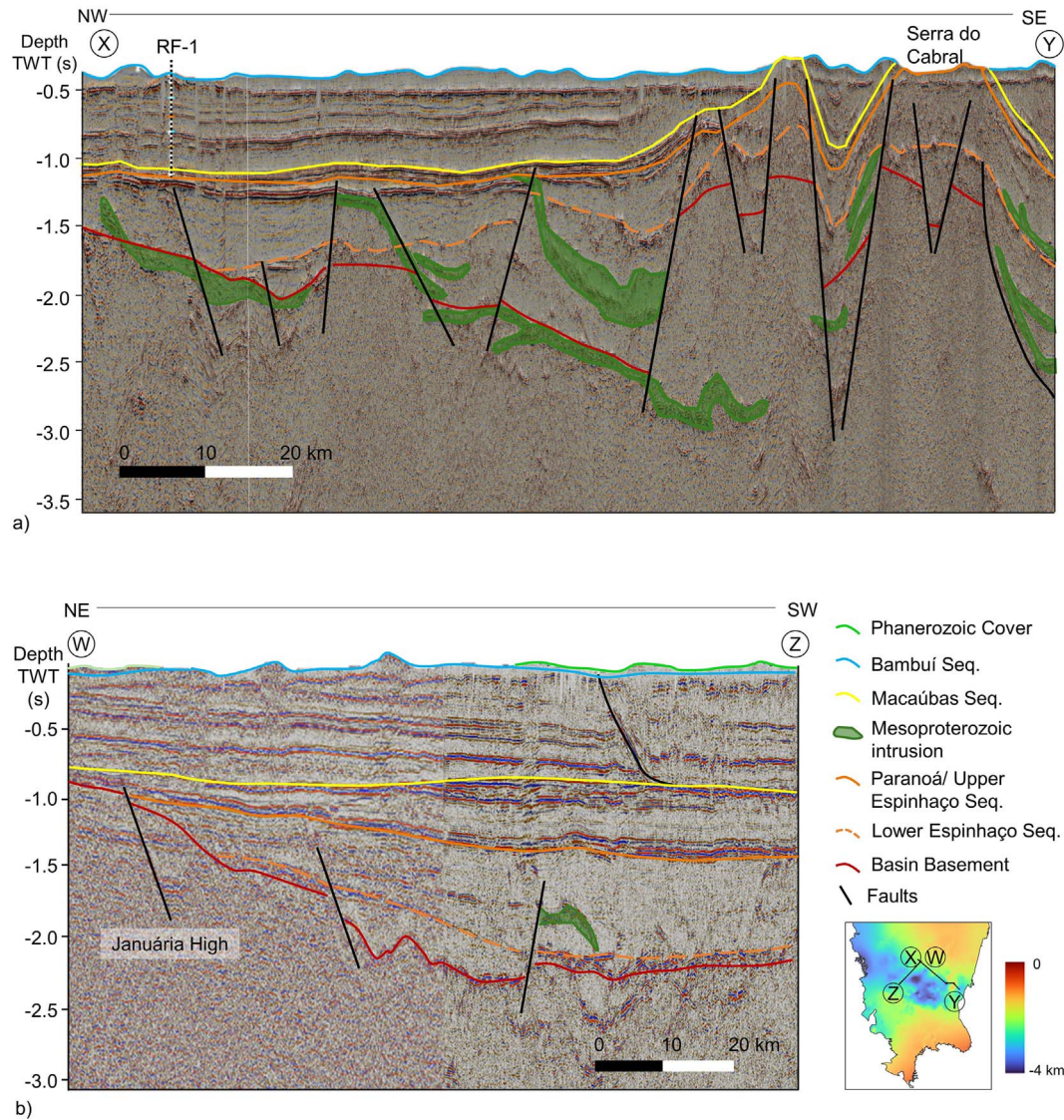
Fig. 5. Seismic profiles of the SFB. (a) Composite seismic line using R0240-STM-0240.0300 and 0319_PETRA_BSF-VIBRO2D_2010_STM_0319-0461, oriented NW-SE. (b) Composite seismic line using R0240-STM-0240.0063 and R0240-STM-0240.0291, NE-SW oriented, showing the Januária High projection.

Lineaments are best identified using the VDR1-THDR-TDR and THGED maps (Figs. 8c and 8d) and some of them are not coincident with the location of faults and other surface structures. Therefore, these features must correspond to basement framework. The VDR1-THDR-TDR map allows visualizing large basement-level structures. Three main directions of lineaments can be recognized: NW-SE, most in the southwest; NNW-SSE, especially in the northeast, and less frequent, NE-SW occurring especially in the central-north.

Furthermore, it should be highlighted that the E-W direction notable feature occurring in the northeast must correspond to a "magnetic artifact" (shown in Figs. 8a, 8c and 8d), probably originating from leveling errors.

In some areas, where the VDR1-THDR-TDR map has low resolution, the THGED map can highlight the lineaments more properly, such as east of the Pirapora anomaly

or in the western part of Quadrilátero Ferrífero, and in the NW portion of the study area.

3.4 Geochemical and isotopic assessment

The gas molecular and isotopic content presented the Table 1 was used to build binary and ternary diagrams to characterize the gas. Similarities and differences between wells and samples were checked, with particular attention to H_2 content.

3.4.1 Gas characterization and isotope signature

The selected four wells present relatively high concentrations of H_2 for two of them (wells PTRA-1 and PTRA-5), whereas the two other wells present lower H_2 concentrations (wells PTRA-2 and PTRA-14). This may be seen in a triangle diagram, where the proportions of the three main
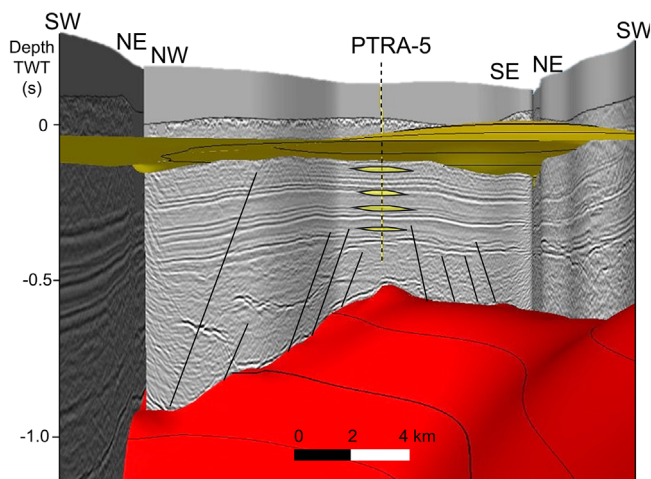
Fig. 6. 3D view of Interpreted time-migrated composite of crooked seismic lines crossed by the well PTRA-5. The well was drilled on a basement high connected by faults to H$_2$-rich layers (lenticular polygon in yellow). Additional legend: Archean/ Paleoproterozoic basement surface in red, Sete Lagoas Formation surface in yellow. Black lines correspond to faults. The lentic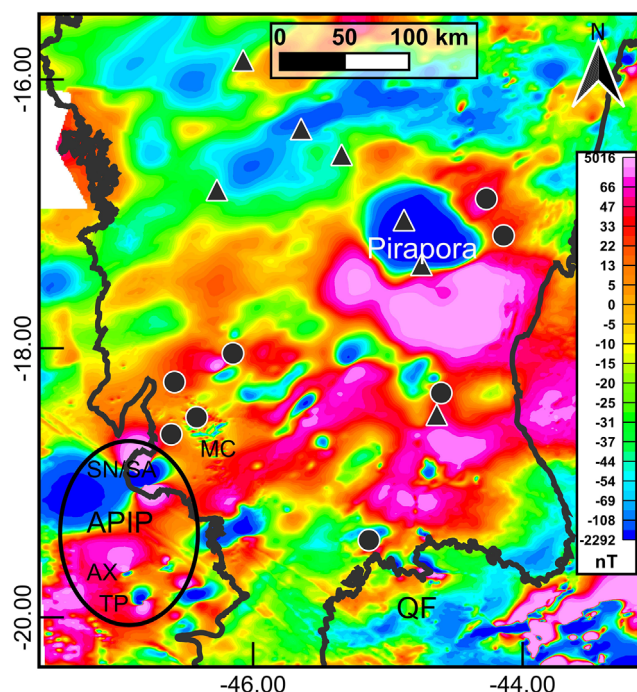ular polygon in yellow is indicative of layers with H$_2$ but does not represent the real thickness and size of these occurrences. Seismic lines 0319-0448, 0319-0449, and 0319-0451 from the 2D seismic survey 0319_PETRA_BSF_ VIBRO2D_2010.

Fig. 7. Total field magnetic anomaly map of the study area. The evident inverse dipole Pirapora anomaly is highlighted in the central part. Other circular and dipolar magnetic anomalies with normal and reversal magnetizations are present in the APIP area. QF= Quadrilátero Ferrífero; MC: Mata da Corda Formation; Alto do Paranaíba Mafic Alkaline Igneous Province (APIP): SN/AS= Serra Negra/Salitre, Ax= Araxá and TP= Tapira. The data used and enhancement methods applied are better described in item 2 of the Appendix.

gas compounds (H$_2$, CH$_4$, and N$_2$) are presented (Fig. 9). The gases from wells PTRA-5 and PTRA-2 present the lowest and highest nitrogen concentrations, respectively, whereas the wells PTRA-1 and PTRA-14 have intermediate nitrogen amounts.

Regarding the carbon isotope, all the gases present "normal" δ^{13}C behavior, with lighter δ^{13}C for the smaller molecule as methane, except the PTRA-1 pattern, that which presents an inversion of the δ^{13}C of methane and ethane (the propane and butane concentrations are too low to obtain reliable isotopic measurements; Fig. 10a).

Additionally, the carbon isotope patterns of the sampled gases present contrasted behavior between the two wells with higher H$_2$ content (PTRA-1 and PTRA-5) and the ones with lower H$_2$ (PTRA-2 and PTRA-14). This may be related to different carbon sources with different δ^{13}C signatures. The two gases without noticeable H$_2$ concentrations present asymptotic δ^{13}C values for C3 and C4 around −40 per mil (Fig. 10a), whereas PTRA-1 and PTRA-5 present much higher values for δ^{13}C, implying an apparent asymptotic value around −25 per mil, even if the butane isotopes could not be measured for the PTRA-1 gases. This isotopic difference between low-H$_2$ and high-H$_2$ gases is also visible in Figure 10b, where the amount of H$_2$ is positively correlated with the isotopic ratios of ethane. It is known that H$_2$ may be reacting in the presence of carbon in order to produce HC: methane through the Sabatier reaction, and C$_{2+}$ molecules through Fisher-Tropsch reactions. As for conventional thermogenic hydrocarbons, the asymptotic value of the δ^{13}C is close to the value of the source, *i.e.*,

the organic matter generated hydrocarbons through thermal cracking. The PTRA-5 gas represents a normal pattern of thermogenic gas generated from an organic source around −25 per mil.

Plotting all the available data with the isotopic ratio of the molecule H$_2$, we may see that their value is relatively constant, between −740 and −620 per mil. This isotopic ratio is negatively correlated with the H$_2$ concentrations (Fig. 11a). This kind of trend may be interpreted as due to a H$_2$ consumption either chemical (alteration) or physical (diffusive loss of a part of the gas, partial dissolution in water): a decrease of its amount is associated, through a Rayleigh distillation process, to heavier values corresponding to the isotopic fractionation of the residual H$_2$. Figure 11b shows that the δD (D/H ratio expressed in per mil) of ethane is positively correlated to the helium concentrations. As helium is associated with sources from the basement, percolating through the sediments of the SFB, its higher concentrations are consistent with a larger generation of ethane through carbon hydrogenation, as an increase of temperature and depth increases the efficiency of the HC generation as well as helium amounts. An increase in ethane generation induces heavier δD, following the inverse Rayleigh distillation process than for H$_2$ alteration, increasing with depth and helium availability.
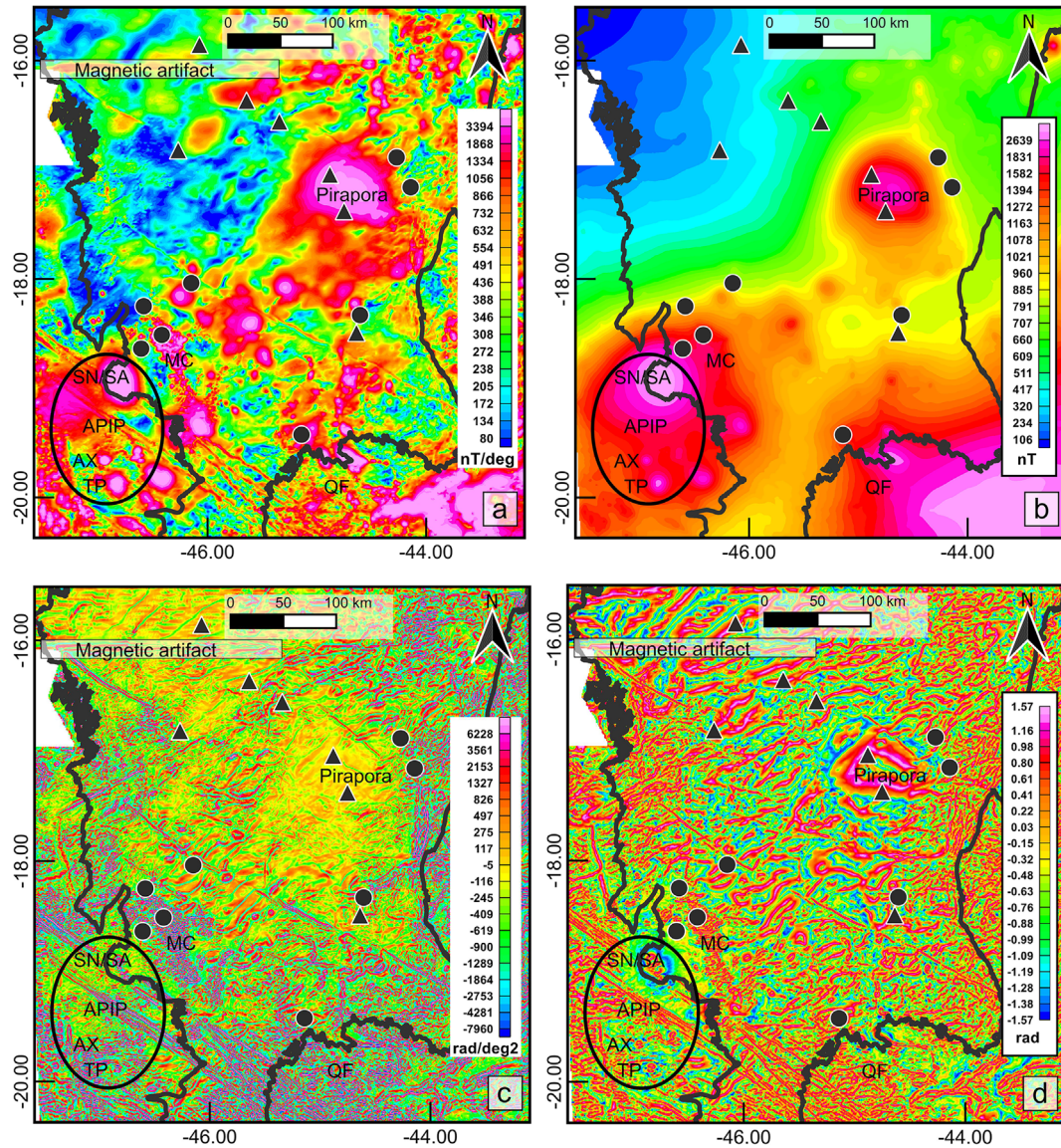
Fig. 8. Enhancement magnetic anomalies maps of the study area. (a) ASA (Analytic Signal Amplitude); (b) VIAS (Vertical Integral of the Analytic Signal); (c) VDR1-THDR-TDR (First Vertical Derivative of the Total horizontal Derivate of the Tilt Angle), and (d) THGED (Tilt Angle of the Horizontal Gradient Enhanced). Black dots correspond to H_2 bearing wells and black triangles to proven H_2 leakage. QF= Quadrilátero Ferrífero; MC: Mata da Corda Formation; Alto do Paranaíba Mafic Alkaline Igneous Province (APIP): SN/AS= Serra Negra/Salitre, Ax= Araxá and TP= Tapira. The data used and enhancement methods applied are better described in item 2 of the Appendix.

The wetness of the HC part of the gases is also clearly separated into two groups: the gases with higher nitrogen amounts (PTRA-1 and PTRA-2) correspond to gases with higher wetness (Figs. 12a and 12b) and larger C2/C1 ratios (Fig. 12c), whereas the gases with lower nitrogen proportions (PTRA-5 and PTRA-14) are associated with drier gases. It appears, for example correlating the C2/C1 ratio with the carbon isotopic ratio of methane (Fig. 12c), that these two gas families cannot be considered as a mixture between two endmembers, but rather as two separated gas families. As a matter of fact, mixing in this diagram would follow a straight line joining the two end members (Prinzhofer and Pernaton, 1997).

As a hypothesis, we assume an isotopic equilibrium between CH_4 and H_2. The equilibrium temperature can then be calculated (Horibe and Craig, 1995). For PTRA-5 this temperature is 80 °C and for PTRA-1 is 125 °C, values much higher than the reservoir temperatures from where these gases have been sampled. Both wells were sampled at a temperature lower than 50 °C. It suggests a dynamic upward migration system that will be discussed later.

In summary, the gas composition of the wells sampled and analyzed in the SFB shows different families, one enriched in H_2, and the other with lower or no H_2 content. The other gas compounds, and their isotopic ratios, show that different processes occurred for the HC and N_2
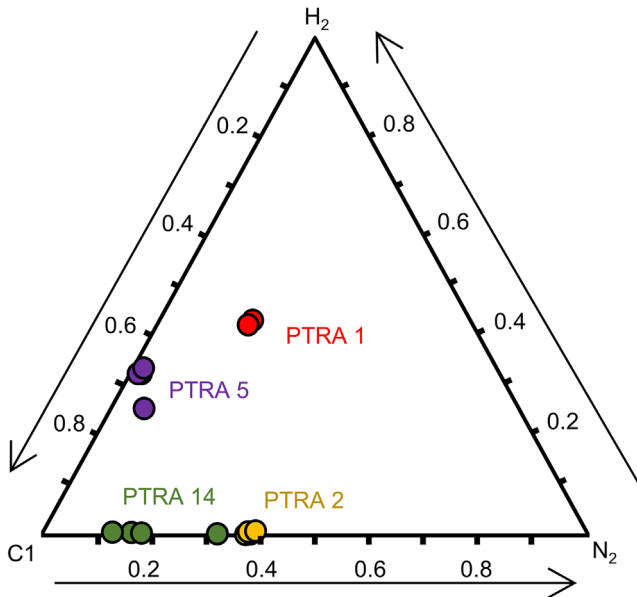
Fig. 9. Triangle diagram with the concentrations of the 3 main gas compounds H_2, CH_4, and N_2 for the 4 studied wells.

generation, whereas the H_2 source, or the H_2 temperature of reequilibrium, looks quite homogeneous, suffering only a partial alteration through HC generation occurring with a hydrogenation of carbon.

3.5 H_2 bearing zone properties

As we just discussed, H_2-rich zones are characterized by a range from 0.07% up to 41% of H_2 content, often associated with high amounts of CH_4 and/or N_2. They are found at different depths, from 300 to 3800 m deep (Table 2). Fine-grained clastic sedimentary rocks, as siltstones and shales, of the Sete Lagoas Formation are the main reservoir lithotypes. However, siliciclastic and carbonate rocks of the Macaúbas, Paranoá and Espinhaço Sequences also contains H_2.

In general, the rocks of these zones are not originally porous, but they present a secondary porosity due to fractures, in most cases filled with calcite or pyrite. They also show very low permeability and transmissibility, according to the available drill stem tests. Some of well tests qualitatively describe the permeability as low or very low. Among the H_2-hosting wells, only well PTRA-2 provides a quantitative permeability value for the well test zone in the Sete Lagoas Formation, which is 0.00784 mD (Table 2).

Other wells, which lack information about the gas composition and thus do not confirm the presence of H_2, provide some data on reservoir properties. According to available petrophysical data, well 1-BRSA-871-MG shows porosity up to 4.3% (with an average of 2.5%) in arenites. In contrast, well 1-BRSA-948-MG exhibits an average porosity of 1% and a permeability of 0.5 mD (with an anomalous value of 7.6 mD) in limestone, both within the Paranoá Group. Well 1-ORT-1-MG indicates a permeability of 0.337 mD and a final static pressure of 1590 MPa, obtained during drill stem tests for the Sete Lagoas Formation.

Regarding the well log interpretation, as in a previous study (Maiga *et al.*, 2023a), the neutron log has been identified as a promising tool for recognizing H_2 presence. The neutron log measures the H_2 index, which indicates the H_2 concentration in a formation (Cannon, 2016). Water and liquid hydrocarbons typically present high neutron readings, whereas for the natural gas the hydrogen index is reduced, resulting in lower neutron readings. In the well data from SFB, we observed a positive correlation between high neutron readings and H_2 layers with an H_2/CH_4 ratio equal or greater than 1 (Fig. 13). When the light HC content (represented only by CH_4 as it constitutes the majority proportion of gaseous hydrocarbons) exceed the H_2 content, the neutron logs are not significantly higher, probably due to impact of low hydrogen index of CH_4. Therefore, in the well PTRA-1, with 41% of H_2, the neutron log peak is mild due to an H_2/CH_4 of about 1.07, while in the well PTRA-13 (about 25% of H_2) is more pronounced, as its H_2/CH_4 is much higher (1.84). In the case of well PTRA-5, despite having substantial amounts of H_2 (33%), the higher CH_4 content (65%) may have masked the effect of H_2 on the neutron logs. The presence of water and liquid hydrocarbons are not listed in these wells, so their possible contribution to higher neutron readings can be excluded. Furthermore, although a positive correlation between high H_2 concentrations and high neutron log readings has been observed in different lithotypes (*e.g.*, sandstone, shale, limestone), more detailed studies can be conducted to evaluate the effect of the matrix on neutron readings in H_2-rich beds.

Neutron logs were used to delineate the H_2-rich zones, revealing a thickness of up to 20 m for the well PTRA-1. Specifically, the well PTRA-12 was estimated at a thickness of 13 m, and for the well PTRA-13 of 5 m. Additionally, the H_2-rich layers are often associated with low density and high sonic log readings (low P-wave velocity). The density log shows low values regardless of its gaseous content, whether it is H_2 or CH_4, as in both cases the presence of the gas reduces the density of the layer. The GR and resistivity logs are not likely to reflect a specific behavior in the H_2-rich layers.

Maiga *et al.* (2023a) also correlated high H_2 concentrations to high values of neutron tool and low readings of density and sonic velocities in carbonate reservoirs from Bourakebougou in Mali. There, the correlation is more remarkable due to higher thickness of the reservoir (tens of meters) and the highest H_2 content (98%).

Although the well logs analysis does not allow distinction between reservoir and seal, since both are tight rocks, it is assumed that the seals may be the interbedded rocks with even lower permeability. Exceptionally, the H_2-rich zone of the PTRA-1 well presents a low GR reading compared to the overlaid layer, indicating the existence of layers with different matrix (Fig. 13). Therefore, the mentioned zone represents the best accumulation among the wells, due to its high H_2 content (41%), in a relatively low depth (around 880 m deep), 20 m of thickness. Additionally, the high neutron and low GR readings can be interpreted as a cleaner matrix reservoir, while the zone above, showing higher GR could correspond to seal rock that prevents or delays the H_2 flux toward the surface.
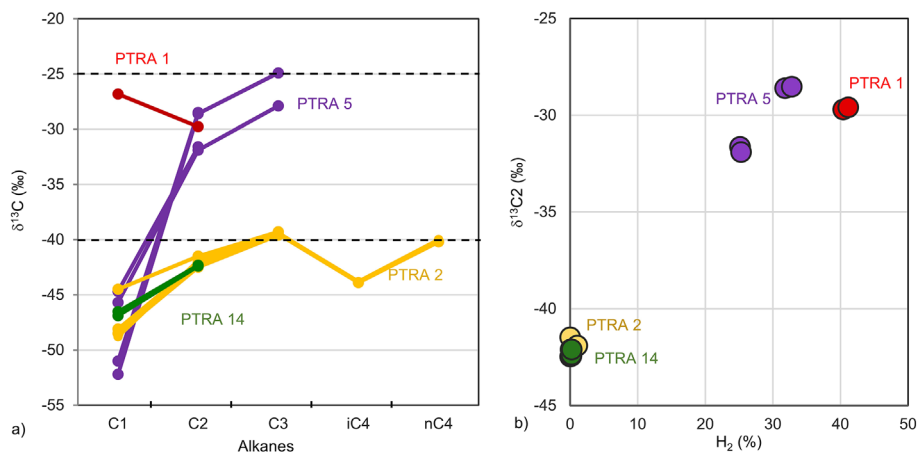
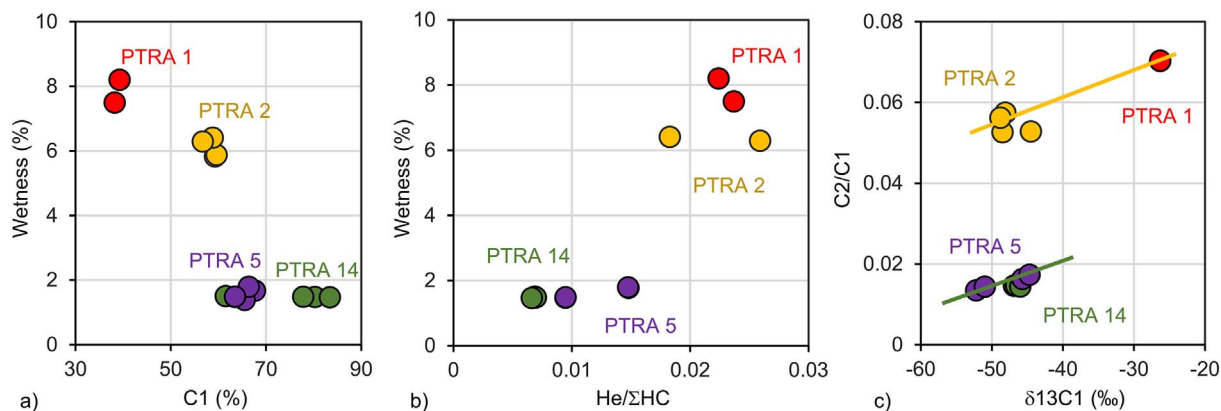**Fig. 10.** Binary diagrams using compositional and isotopic data from the wells PTRA-1, PTRA-2, PTRA-5, and PTRA-14. (a) carbon isotopic patterns of HC gas compounds C1 to C4, the two horizontal dashed lines correspond to asymptotic δ13C values around -15 and -40 per mil; (b) Correlation between the carbon isotopic ratio of ethane and the H_2 concentrations.
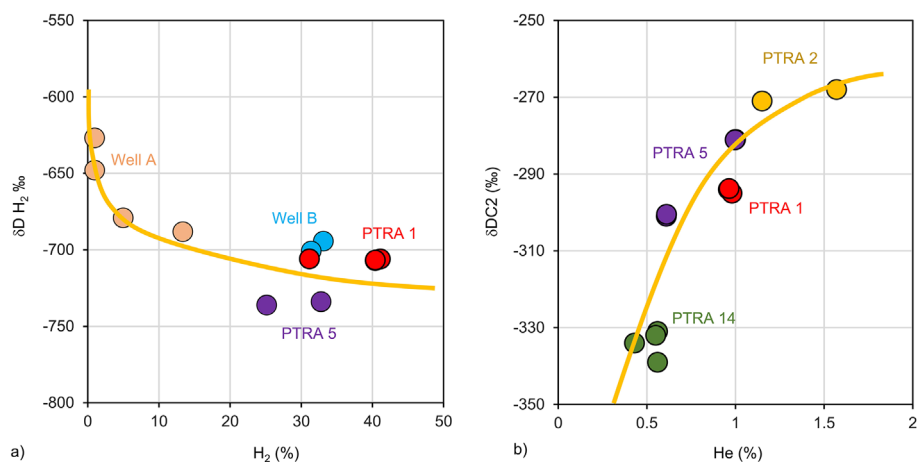
Fig. 11. Binary diagrams using compositional and isotopic data from the São Francisco Basin wells. (a) Correlation between the concentration of H_2 and its isotopic ratio; (b) Correlation between the H_2 isotopic ratio of ethane versus the helium concentration of the gases. The wells A and B are located inside the study area and their data come from Prinzhofer's private dataset and are not discussed in this article, as they do not correspond to the public data provided by the Brazilian institutions. They were added to the figure solely to better illustrate the H_2 consumption.

Fig. 12. Binary diagrams using compositional and isotopic data from the wells PTRA-1, PTRA-2, PTRA-5, and PTRA-14. (a) Correlation of gas wetness (C2-C5/C1-C5) in percentage versus the concentration of methane; (b) Correlation of gas wetness versus the proportion of helium normalized with the sum of hydrocarbons; (c) Correlation of the ratio ethane/methane versus the carbon isotopic ratio of methane.

Table 2. H_2-rich zone description based on available well log information from eight exploratory wells. *H_2 zone thickness not estimated due to low neutron reads. **We show the original values in ppm, but they could not correspond to the exactly H_2 amount in the zone, because they correspond to isotube or isojar samples, which do not have the same reliability as cylinder samples. To emphasize the cylinder well test data, additional layers with reported H_2 in the PTRA-1, PTRA-2, and PTRA 5 datasets were not listed in the table due to their unreliable origin (isojar samples).

Well	Range of depth with H_2 (meters deep)	Main lithotype	Sequence/ Lithostratigraphy	H_2 amounts (max)	Reservoir properties
PTRA-1	860 to 912 (Cylinder – well test)	Siltstone and shale	Sete Lagoas Fm	41.1%	Pores closed and fractures filled with calcite. Drill stem tests indicate a reservoir with very low permeability, final static pressure around 14.4 MPa (about 2090 psi) and not depleted.
PTRA-2	1790 to 1930 (Cylinder – well test)	Siltstone and calcarenite	Sete Lagoas Fm	1.0%	Microfractures filled with calcite. Well tests suggest a reservoir with a low permeability of 0.00784 mD and final static pressure of 170,78 gf/cm^2, approximately 2430 psi.
PTRA-5	348 to 509 (Cylinder – well test)	Siltstone and shale	Sete Lagoas Fm	32.8%	Fractures filled with pyrite. Final static pressure measure during the wireline formation test: 4.9 MPa, approximately 722 psi.
PTRA-6	900 to 1008	Arenite and phyllite	Macaúbas and Espinhaço Sequences	36,100 ppm**	Presence of veins on arenite and foliation on phyllite.
PTRA-10	1203 to 1311	Calcarenite	Macaúbas Sequence	67,300 ppm**	Presence of fractures. Drill stem tests indicate a reservoir with very low permeability and final static pressure of 13.7 MPa, approximately 1984 psi.
PTRA-12	2450 to 2950, 3565 to 3850	Calcilutite and calcarenite, marl and dolomite	Sete Lagoas Fm, Macaúbas and Paranoá Sequences	229,800 ppm**	No primary porosity. Presence of fractures.
PTRA-13	954, 1670 to 2604, 2712 to 2784	Shale, claystone and arenite	Bambuí Grp, Sete Lagoas Fm and Paranoá Sequence	244,600 ppm**	Presence of four types of microfractures: opened, cemented, filled with calcite, and with quartz.
PTRA-14	1779 to 1929 (Cylinder – well test)	Siltstone and calcilutite	Bambuí Sequence and Sete Lagoas Fm	0.2%	Microfractures and stylolites, showing porosity lower than 1% (based on petrography analysis). Drill stem tests indicate a reservoir with very low permeability and final static pressure of 14.3 MPa, about 2076 psi).

4 Discussion

4.1 H_2 indices and H_2 exploration

The dataset presented in this paper allows a regional view of H_2 within the SFB. Often, the only elements available to start evaluating a zone are the presence of potential H_2-generating rocks and surface seepages such as gas seeps on faults or SCDs. Due to previous HC exploration and the richness of the mineral provinces, the amount of subsurface data on the SFB is large and allows us to rank the usefulness of the indices. For instance, as for the oil and gas seeps, the absence or presence of SCDs clearly can be interpreted in different ways. Their presence can indicate that the H_2
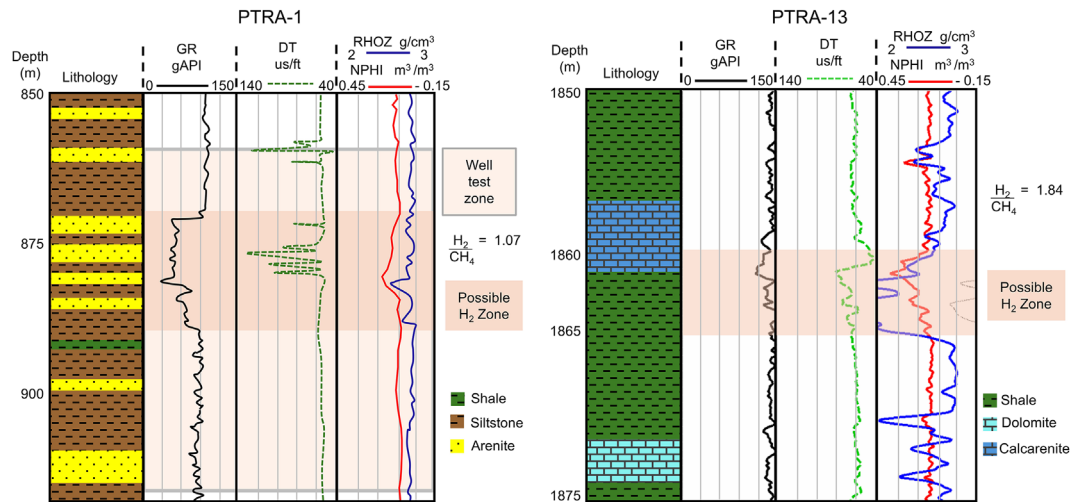
Fig. 13. Gamma Ray (GR), Sonic (DT), Density (RHOZ) and Neutron (NPHI) logs for the wells PTRA-1 and PTRA-13, focusing on layers with amounts of H_2 higher than methane ($H_2/CH_4 > 1$). The main lithology description was assumed based on sidewall and core samples. *Dark pink zones present high neutron and low density, then interpreted as H_2 zones.

system is working or that the seal is missing or not efficient, allowing leaks.

At the basin scale, SCDs distribution when faced with the geological map exposes an evident correlation with Cenozoic cover (Fig. 14). Additionally, some areas with H_2 presence confirmed by H_2 bearing wells are not surrounded by SCDs (PTRA-2, 5, 12, 14), while others, located over Cenozoic covers (PTRA-6), are surrounded with SCDs. It is noticeable that some soils allow the formation of visible SCDs, some others do not. In the SFB, their number and footprint seem primarily influenced by the soil and near-surface formations. These characteristics must be considered before relating H_2 generation with the absence or, on the contrary, the large number of SCDs. In particular, the lack of SCD cannot be used to rule out the existence of natural H_2 in any area.

In addition, most of SCDs with confirmed H_2 reported by Moretti *et al.* (2021b) are concentrated in the central part of the basin, situated on Cenozoic covers with minimal deformation (Alkmim and Martins-Neto, 2001), and sometimes coincide with alignments of normal faults (Fig. 4). In contrast, the wells containing H_2 are predominantly located in the deformed zones affected by the Araçuaí and Brasília thrust belts, on Neoproterozoic units and, to a lesser extent, Cretaceous units.

The presence of H_2 in the soil without SCD has been already noticed in the Pyrenees (Lefeuvre *et al.*, 2022), above the field of Bourakebougou in Mali (Prinzhofer *et al.*, 2018), and in a wet tropical climate, such as part of Colombia, where H_2 emanations are visible in a different way since the vegetation does not disappear (Carrillo *et al.*, 2023). Near outcropping faults, features that focus the gas circulation, and SCDs are not apparent either (Pasquet *et al.*, 2022; Prinzhofer *et al.*, 2024). The more regional approach developed here clearly highlights the key role of the soil and outcropping formations in the growth of these depressions. These considerations are complementary to the fact that the presence of seals can result in the absence of a migration path to the surface.

4.2 H_2 systems in the SFB

The SFC is a prolific area for H_2 due to the presence of various iron-rich facies from both mantellic and sedimentary origin and K-rich granites, as well as deep faults, reservoirs, and traps. Therefore, the main elements of the H_2 system are present. Nonetheless, the information provided shows the SFB is non-uniform in terms of H_2 potential and suggests that more than one H_2 system is active, even though the geochemical data is consistent and indicates some homogeneity in terms of H_2 generation reactions. Since the H-isotopes of H_2 equilibrate rapidly, alone this value does not allow definition of H_2 origin source nor depth, more likely it will indicate a depth where the H_2 is stored, as free gas or dissolved in an aquifer (Lévy *et al.*, 2023).

4.2.1 Potential generating rocks

In the SFB and its surrounds, outcrops of ultramafic rocks and BIFs as well the presence of magnetic anomalies correspond to favorable factors for H_2 generation through the hydration process of iron-rich rocks. Outside the southern portions of the SFB, Archean and Paleoproterozoic BIF are present in the QF and Neoproterozoic BIF outcrop on the eastern side. To the west, iron-rich facies are related to the intrusions in the Alto do Paranaíba Igneous Province. Iron-rich rock occurrences are suggested by the presence of magnetic anomalies inside the São Francisco Basin and it surrounds, such as the Pirapora, QF, and APIP anomalies. Moreover, other magnetic anomalies were identified as smaller bodies located in the north (Januária High) and southwest of the Pirapora anomaly, probably corresponding to the subsurface expression of ferrous/ferric rocks and pipe-type bodies, respectively. Furthermore, the contribution to the H_2 generation of radioactive-rich granitoids cannot be ruled out. The presence of helium (from 0.6 to 1.6%) with a crustal signature ($^3He/^4He < 0.02$ R/R_A; Flude *et al.*, 2019) associated with the H_2 layers point to a possible contribution of rocks hosting radioactive
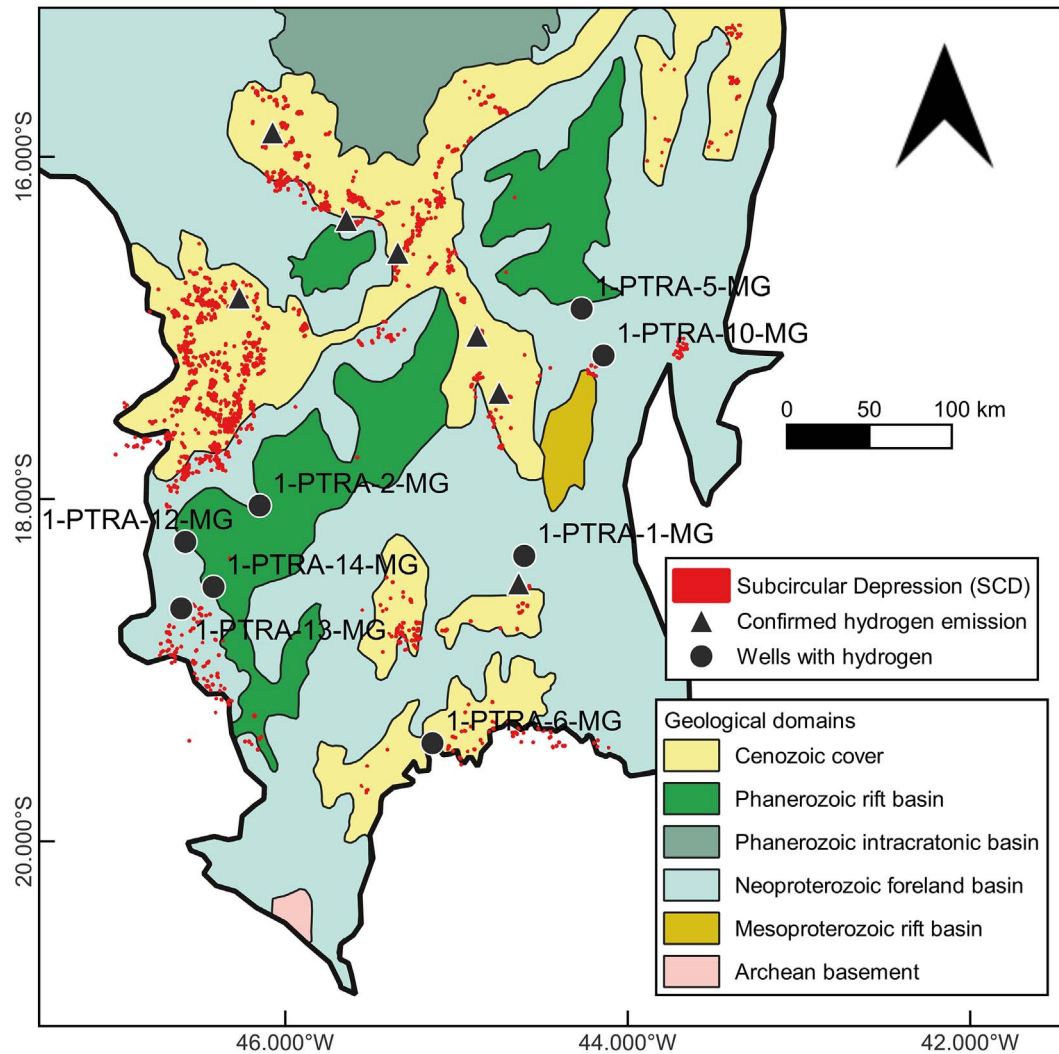
Fig. 14. Geological map of the study area with SCDs mapped. Although potential sources of H$_2$ are widespread, most of the SCDs was observed in the Cenozoic cover outcrops, indicating these soft sediments present favorable conditions for SCD formation. Geological domains from Delgado *et al.* (2003) and Garayp and Frimmel (2022).

elements, *e.g.*, TTG and K-rich granites, as secondary H$_2$ generating rocks. The location of these rocks in the SFB basement is uncertain, as they outcrop only in the São Francisco Craton, but not within the basin.

4.2.1.1 Central/east part
In this region, the wells with the highest H$_2$ amounts (PTR-1 and PTR-5) and some proven H$_2$ emanations were found, it can therefore be considered a high-potential region for H$_2$ exploration. The H$_2$ may come from the BIF, Archean/ Paleoproterozoic or Neoproterozoic. In addition, although the lack of outcropping ultramafic bodies, magnetic anomalies are found in the central part of the SFB (Figs. 7 and 8), the most expressive corresponds to the Pirapora anomaly.

The H$_2$ potential of the Pirapora magnetic anomaly, in the central-eastern part of the study area, has been suggested by Donze *et al.* (2020). This body is very likely extremely iron-rich (Figs. 7 and 8), as discussed previously; its depth is uncertain but probably very deep. This great depth raises the question of the water availability and also tem-

perature. Following the experiment done by Klein *et al.* (2013), the dunite serpentinization is fast around 300 °C but drops very quickly above 360 °C. For the SFB, considering a 20 °C/km gradient, the serpentinization temperature window would be between 14 and 17 km (using a surface temperature of 20 °C). If a 25 °C/km gradient from the well PTRA-5 is used, the temperature window is from 11 to 13.5 km. Similarly, Donze *et al.* (2020) with the same gradient suggest a H$_2$ generation of around 10–12 km. Although the question is not fully solved, the Pirapora anomaly could be a probable H$_2$ kitchen (Fig. 15), however, the fact that the magnetic data suggests a deep body for a large part at temperature too high to allow H$_2$ generation must be taken into account.

4.2.1.2 Southern part
In the southern basin, magnetic anomalies could indicate the subsurface continuity across parts of the SFB of the BIFs and ultramafic rocks, which outcrop the QF. They also correspond to potential H$_2$ kitchen, even at shallow
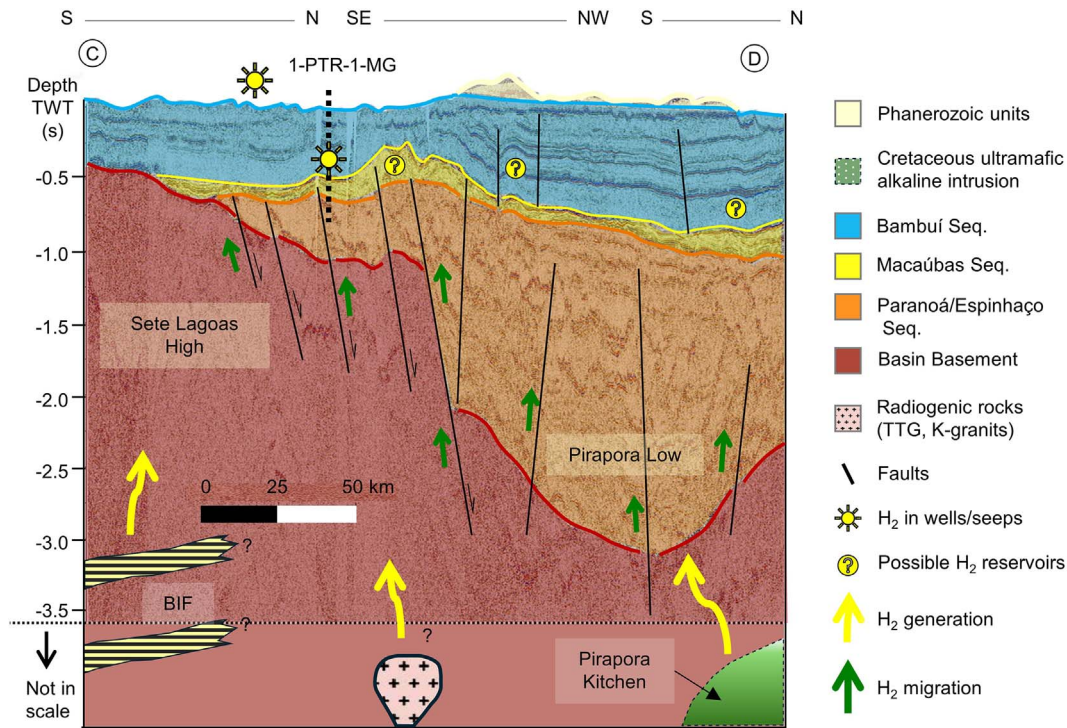
Fig 15. Sketch of the potential H$_2$ kitchen for the southern part of the SFB: southward the BIF overthrusted in the belts, the intrusions, and the Pirapora magnetic anomaly. The vertical scale is in time for the seismic lines and schematic for the deepest part.

depths, given the capacity of magnetite found in the BIF to generate H$_2$ at low temperatures (<200 °C, Geymond *et al.*, 2023). The volume of generating rocks, however, has not been widely tested, only a couple of wells are available in this area, one of them with H$_2$ (PTR-6), the mines are mainly open pits, and the subsurface geometry is poorly defined.

4.2.1.3 Western part

To the southwest of the SFB ultramafic intrusions are exposed, including kimberlite, containing mantle rocks that could generate H$_2$. They are very rich in olivine, even if this mineral is mainly enriched in magnesium where outcropping (Fernandes *et al.*, 2021). The intrusions are numerous and await a volumetric approach.

The intrusions (Salitre, Serra Negra, Araxá, and Tapira) and extrusion rocks (Mata da Corda Formation) of the ultramafic alkaline province correspond to APIP. This area also presents relevant magnetic anomalies, suggesting a deep expression of that ultramafic magmatism.

Four wells with H$_2$ were drilled in the western portion of the SFB (PTRA-2, PTRA-12, PTRA-13, and PTRA-14) and SCDs are abundant, suggesting an active area for H$_2$ generation.

An additional generating rock could theoretically be the overmature source rocks from the Bambuí Fm. The more than 600 m of overmature source rocks drilled near the surface surely extend deeper, even if it is difficult on the seismic lines to know up to which depth. The maximum of maturation has been reached 600 Ma ago (Fig. 2), hence their role in the current H$_2$ flow is therefore questionable.

4.2.1.4 North

The Januária area displays many SCDs, some of them with proven H$_2$ emanation, suggesting the presence of H$_2$ generating rock. However, the absence of H$_2$ found in the exploratory well drilled there (PTRA-7) suggests a lower H$_2$ generation potential or the absence of effective traps and seals.

4.2.2 Migration pathways

The available data raise a question about the mode and distance of H$_2$ transport. Looking at the location of the kitchens and the H$_2$ shows and indicators (*e.g.*, SCD, Fig. 14), we proposed several possible migration routes in the basin, from long and short distances, both vertical and horizontal (Fig. 16). Additionally, it is expected an upwards H$_2$ migration especially through faults, once the degree of compaction of old sedimentary sequence of the basin are high. However, the small size and diffusive character of the H$_2$ molecule can result in flux even in tight formations.

The NW-SE Proterozoic rift structures must correspond to the most important migration route at the pre-Bambuí level. They were active during the deposition of the Paranoá-upper Espinhaço sequence and may have been reactivated in the Neoproterozoic Era, during the Macaúbas and Bambuí sequence deposition (Reis and Alkmim, 2015). During and after the Neoproterozoic, fault system, N-S oriented, associated with thrust-belt generation in western and eastern edges of the basin should provide reliefs and migration pathways inducing fluid circulation in the deeper sequences of the basin.
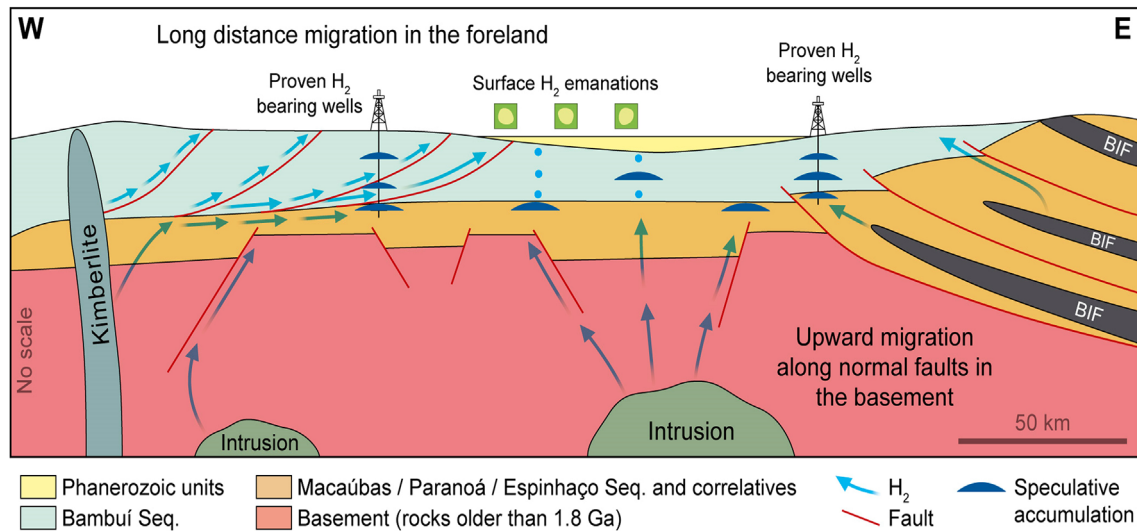
Fig. 16. Schematic regional geological profile crossing central-southern São Francisco Basin with the elements of H$_2$ system. Lithostratigraphic units and faults interpreted based on composite of seismic lines and wells. Basement H$_2$ generating rocks based on regional geological understanding and magnetic anomalies.

Cretaceous extensional events that originated alkaline intrusions and NW-SE dyke swarms, recognized on magnetic maps (Figs. 7 and 8), especially in the southwestern basin, also represent a possibility of the fluid ascension from deep to shallow levels.

In the north-western portion of the study area, the large SCD presence and confirmed H$_2$ seeps, where no H$_2$-generating rocks have been outlined so far, necessitate a long-distance migration. In the area there is an important set of faults, roughly N-S to NW-SE orientation with east-verging thrust system, which could provide the pathway for H$_2$ migration over long distances from a source outside the basin.

If we consider the Pirapora anomaly as the main H$_2$ kitchen also for the areas of wells PTR-2 and PTR-14, a long-distance migration is required. On the other hand, in the ultramafic alkaline province and Quadrilátero Ferrífero, the source may be at a shallower level, requiring shorter vertical distances migration.

4.2.3 Traps and seals

Due to the two orogens, traps are mainly structural in the SFB. The majority of the traps are four-way dip closures associated with reactivated Archean and Proterozoic structures, or Neoproterozoic belt orogen. One may suppose that stratigraphic traps exist but the quality of the seismic and the lack of 3D seismic do not allow their definition.

Except for the Cenozoic cover, all the rock units are tight and the differences in lithology between reservoirs and seals appear to be minimal, making geophysical logs such as GR often inefficient for distinguishing them. At least for the HC industry, which previously targeted these tight reservoirs, only slight variations in permeability differentiate the reservoir from seal layers.

From the existing data, seals in the São Francisco Basin consist of very fine-grained rocks devoid of primary and secondary porosities, which are interbedded with slightly more permeable layers within the same lithostratigraphic units. Mesoproterozoic and Cretaceous intrusions may also act as a seal due to their typically non-porous nature and stacked geometry favoring trap formation, although further studies are required to confirm their potential.

The lower prevalence of SCDs in the areas of H$_2$-rich wells could be attributed to efficient sealing mechanisms. Nevertheless, these areas are also characterized by the absence of unconsolidated sedimentary covers (Fig. 14). Thus, as previously discussed in Section 4.1, the absence of SCDs directly above well zones does not necessarily imply an absence of H$_2$ seeps, but rather that they may not be detectable on the type of sedimentary covers.

4.2.4 Uplift and H$_2$ generation and/or degassing

The presence of a Proterozoic trap hosting H$_2$ is compatible with a past generation and accumulation in the basin. However, generation can be also active today. We suspect that the uplift of the area plays a key role here and on the global stage (Moretti *et al.*, 2021a; Prinzhofer *et al.*, 2019). Fission Track data shows that the Araçuaí Belt has undergone continuous uplift over at least the past 300 Ma and temperatures have dropped by more than 100 °C (Fonseca *et al.*, 2021). The same authors described the uplift as even longer within the Brasília Belt, and at the opposite, in the São Francisco Basin (referred SFC by these authors) the denudation could be more recent, but its rate accelerates during the last 10 Ma. As a result, temperatures decreased in the basin by more than 50 °C. Considering a gradient of 25 °C, it means that a thickness of 2 km of deep material could has recently reached the H$_2$ generation window. So, there may be a current H$_2$ generation throughout the basin and belts, even if the rocks and shortening tectonics are very old. This massive erosion can also lead to dysmigration and degassing of previously trapped, or adsorbed, gases.

The high adsorption capacity of the clay minerals has been highlighted by previous studies (Truche *et al.*, 2018) and will result in desorption in case of erosion and pressure decrease. Today, the basin modeling tools for H_2 are still on their infancy, we cannot really quantify the influence of this denudation. However, the SFB is the only area where H_2 flow monitoring in the soil has been done, for almost 2 years, allowing the use of this key dataset.

As a rough estimation, the SCDs monitored previously (Moretti *et al.*, 2021a, Prinzhofer *et al.*, 2019) show an H_2 emanation of about 700 kg/day which means about 250 t/yr. In this study, without trying to be exhaustive, we mapped 1900 other SCDs with close characteristics, which means 475,000 t/yr if the flow rate is similar. Donze *et al.* (2020) highlighted this apparent discrepancy between the current flow and the rate of H_2 generation they computed. They were only considering the radioactivity, and the ultramafic rocks so disregarded the role of the BIFs as generating rocks. In addition, no consideration was given to either the hypothesis of dysmigration and/or current leakage due to the denudation. In our view, these new elements make all these data compatible in a global system that is much more dynamic, and more complex, than the one previously proposed.

Of course, there is no proof that all these SCDs have the same leakage rate, but this figure gives an idea of the enormous amount of degassing currently taking place in this basin. Unlike HC source rocks, where a high temperature will make the organic matter completely overmature, a high temperature inhibits oxidation and promotes the generation of H_2. As a result, the Mesozoic uplift and especially the Quaternary fast uplift brings into the H_2 generation window these deep rocks that were previously excluded because they were too hot.

5 Conclusion

H_2 exploration in the SFB has already started. Soil gas measurement and geophysical and wells data analysis confirm the presence of the main elements of the H_2 system: generating rocks, migration, reservoir, seals, and traps. The massive presence of ancient rock complexes, especially from the Archean and Proterozoic, formed in redox conditions and many radioactive elements, make the SFB a very favorable area for H_2 generation.

Multiphase structural history allows short and long-distance migration of gas in the basin, even from very deep sources. A complex burial process results in the presence of tight formations, with low permeability, which acts as a good seal, however, this is a concern to the reservoir properties. Well tests focusing on H_2 production must be done to properly evaluate the H_2 reservoirs.

Only two of the eight wells containing H_2 and a small ratio of proved H_2 surface emissions are located over or close to the Pirapora magnetic anomaly, suggesting that this feature is not the main H_2 generating zone in the SFB. Four of the H_2 bearing wells are located near the kimberlite/ ultramafic intrusion zone (APIP, westward), and one is near the QF, which is also a magnetic anomaly. Most of these places are not coincident with the SCD high-density zones, which suggest the presence of impermeable rocks may be able to prevent or delay the ascending flow of gas towards the surface, acting as a seal for H_2. Alternatively, the absence of SCD may be due to soil rheology rendering impossible the formation of topographic depressions.

The basement is cut by normal faults bordering deep grabens and intruded by Cretaceous ultramafic bodies, westward, and BIFs and Proterozoic iron-rich rocks in the south and eastward. In general, the lithotypes are tight and the main migration path is considered to be associated with fault zones. On the other hand, the Proterozoic compressive structures and the double foreland are in complete disharmony, with roughly N-S faults with E-W gently dipping beds that may favor long-distance migration. The structural traps are within these thrusts and the BIF and ultramafic bodies, involved in the thrust in the two mountain belt areas, could be the H_2 kitchen.

Despite the data acquired so far in the basin, its hydrogen exploration knowledge is still very incipient. Extra activities can be now conducted, such as:

- Verification if extra H_2 data can be offered by the HC industry, such as compositional gas analyses, as if they exist. These data were not provided by the companies to ANP for around 35% of exploratory wells drilled in the São Francisco Basin.
- New seismic line acquisition, mainly in the basin border, is affected by the compression, due to their high potential for discoveries and the lack of proper seismic surveys covering.

The natural H_2 exploration activity in Brazil was recently approved by Law N°. 14.948/2024 and is only awaiting the publication of specific resolutions to become a reality.

After overcoming economic and legal barriers, other activities can be performed:

- Revisiting the wells, carrying out gas sampling and analysis, as well as production testing.
- Drilling new exploratory wells, choosing the southeastern compressive structures (from PTRA-5 northward to PTRA-6 southward) as a first target area, since this area is close to various potential H_2-generating rocks and migration routes.
- Test the wells if shows are found: long-term production test from the wells with proven H_2 is the most crucial missing data enabling increased confidence in the economic value of the H_2 flow.

Once discoveries are made, the existing gas pipeline network connecting the southern São Francisco Basin to the largest population centers in the Brazilian states of São Paulo, Rio de Janeiro, and Minas Gerais (about 80 million people) can promote future H_2 production and distribution.

Acknowledgments

Conflicts of interest

The authors declare that they have no known competing financial interests or personal relationships that could have appeared to influence the work reported in this paper.

Supplementary material

The supplementary material of this article is available at https://stet-review.org/10.2516/stet/2024091/olm.

Table. Public and available compositional and isotopic data from wells drilled in the study area in the São Francisco Basin, Brazil.

References

Alkmim F.F., Martins-Neto M.A. (2001) A Bacia Intracratônica do São Francisco: Arcabouço estrutural e cenários evolutivos, in: Pinto C.P., Martins-Neto M.A. (eds), *Bacia do São Francisco: Geologia e Recursos Naturais*, Sociedade Brasileira de Geologia (SBG) – Núcleo MG, Belo Horizonte, pp. 9–30.

Amaral L., Caxito F. A., Pedrosa-Soares A. C., Queiroga G., Babinski M., Trindade R., Lana C., Chemale F. (2020) The Ribeirão da Folha ophiolite-bearing accretionary wedge (Araçuaí orogen, SE Brazil): New data for Cryogenian pla-giogranite and metasedimentary rocks, *Precambrian Res.* **336**, 105522. https://doi.org/10.1016/j.precamres.2019.105522.

Assumpção M., Azevedo P.A., Rocha M.P., Bianchi M.B. (2017) Lithospheric Features of the São Francisco Craton, in: Heilbron M., Cordani U., Alkmim F. (eds), *São Francisco Craton, Eastern Brazil. Regional geology reviews*, Springer, Cham, pp. 15–25. https://doi.org/10.1007/978-3-319-01715-0_2.

Boreham C. J., Edwards D. S., Feitz A. J., Murray A. P., Mahlstedt N., Horsfield B. (2023) Modelling of hydrogen gas generation from overmature organic matter in the Cooper Basin, Australia, *APPEA J.* **63**, 2, S351–S356. https://doi.org/10.1071/AJ22084.

Borges A.J., Drews M.G.P. (2001) Anomalias Aeromagnéticas Notáveis da Bacia do Rio São Francisco, in: Seventh International Congress of the Brazilian Geophysical Society, Salvador, 28–31 October, European Association of Geoscientists & Engineers, pp. 742–745. https://doi.org/10.3997/2214-4609-pdb.217.183.

Brandt A. R. (2023) Greenhouse gas intensity of natural hydrogen produced from subsurface geologic accumulations, *Joule* **7**, 8, 1818–1831. https://doi.org/10.1016/j.joule.2023.07.001.

Cannon S. (2016) *Petrophysics: a practical guide*, John Wiley and Sons, Ltd, ISBN 978-1-118-74674. https://doi.org/10.1002/9781119117636.

Carrillo A.R., Gonzalez Penagos F., Rodriguez G., Moretti I. (2023) Natural H_2 emissions in Colombian ophiolites: first findings, *Geosciences* **13**, 12, 358. https://doi.org/10.3390/geosciences13120358.

Delgado I.M., Souza J.D., Silva L.C., Filho N.C.S., Santos R.A., Pedreira A.J., Guimarães J.T., Angelim L.A.A., Vasconcelos A.M., Gomes I.P., Filho J.V.L., Valente C.R., Perrota M.M., Heineck C.A. (2003) Geotectônica do Escudo Atlântico, in: Bizzi L.A., Schobbenhaus C., Vidotti R.M., Gonçalves J.H. (eds), *Geologia, Tectônica e Recursos Minerais do Brasil*, CPRM, Capítulo V, Brasília, pp. 227–258.

Dignart A. (2013) São Francisco basin, in: *Brasil Round 12th – Oil and gas bidding rounds*, Agência Nacional do Petróleo, Gás Natural e Biocombustíveis, Available at https://www.gov.br/anp/pt-br/rodadas-anp/rodadas-concluidas/concessao-de-blocos-exploratorios/12a-rodada-licitacoes-blocos/arquivos/seminarios/sao-francisco.pdf (accessed March 5, 2024).

Donze F, Truche L, Shekari Namin P, Lefeuvre N, Bazarkina E. (2020) Migration of natural hydrogen from deep-seated sources in the Sao Francisco basin, Brazil, *Geosciences* **10**, 346. https://doi.org/10.3390/geosciences10090346.

Fernandes P.R., Tommasi A., Vauchez A., Neves S.P., Nannini F. (2021) The São Francisco cratonic root beneath the Neoproterozoic Brasilia belt (Brazil): Petrophysical data from kimberlite xenoliths, *Tectonophysics* **816**, 229011. https://doi.org/10.1016/j.tecto.2021.229011.

Fonseca A.C.L., Novo T.A., Nachtergaele S., Fonte-Boa T.M.R., Van Ranst G., De Grave J. (2021) Differential phanerozoic evolution of cratonic and non-cratonic lithosphere from a thermochrono-logical perspective: São Francisco Craton and marginal orogens (Brazil), *Gondwana Res.* **93**, 106–126. https://doi.org/10.1016/j.gr.2021.01.006.

Frery E., Langhi L., Maison M., Moretti I. (2021) Natural hydrogen seeps identified in the North Perth basin, Western Australia, *Int. J. Hydrog. Energy* **46**, 61, 31158–31173. https://doi.org/10.1016/j.ijhydene.2021.07.023.

Flude S., Warr O., Magalhaes N., Bordmann V, Fleury J. M., Trindade R., Reis H., Sherwood Lollar B., Ballentine C. (2019) Deep crustal source for hydrogen and helium gases in the São Francisco Basin, Minas Gerais, Brazil, in: *AGU Fall Meeting Absracts.* Available at https://agu.confex.com/agu/fm19/meetingapp.cgi/Paper/534136.

Garayp E., Frimmel H.E. (2022) A modified paleoplacer model for the metaconglomerate-hosted gold deposits at Jacobina, Brazil, *Miner Depos.* **59**, 627–654. https://doi.org/10.1007/s00126-023-01220-9.

Geymond U., Ramanaidou E., Lévy D., Ouaya A., Moretti I. (2022) Can weathering of banded iron formations generate natural hydrogen? Evidence from Australia, Brazil and South Africa, *Minerals* **12**, 163. https://doi.org/10.3390/min12020163.

Geymond U., Briolet T., Combaudon V., Sissmann O., Martinez I., Duttine M., Moretti I. (2023) Reassessing the role of magnetite during natural hydrogen generation, *Front. Earth Sci.* **11**, 1169356. https://doi.org/10.3389/feart.2023.1169356.

Gibson S.A., Thompson R.N., Leonardos O.H., Dickin A.P., Mitchell J. (1995) The Late Cretaceous impact of the Trindade mantle plume: evidence from large-volume, mafic, potassic magmatism in SE Brazil, *J. Petrol.* **36**, 189–229. https://doi.org/10.1093/petrology/36.1.189.

Guélard J., Beaumont V., Rouchon V., Guyot F., Pillot D., Jézéquel D., Ader M., Newell K.D., Deville E. (2017) Natural H_2 in Kansas: deep or shallow origin? *Geochem. Geophys. Geosyst.* **18**, 1841–1865. https://doi.org/10.1002/2016GC006544.

Guimarães S.N.P., Prado E.M.G., Viera F.P., Lacasse C.M., Rocha N.S., Jesus B.L., Souza Filho O.A. (2022) Updated mapping of terrestrial heat flow in Brazil, *J. South Am. Earth Sci.* **113**, 103627. https://doi.org/10.1016/j.jsames.2021. 103627.

Hackspacher P. C., Ribeiro L. F. B., Ribeiro M. C. S., Fetter A. H., Neto J. H., Tello C. E. S., Dantas E. L. (2004) Consolidation and break-up of the South American platform in southeastern Brazil: tectonothermal and denudation histories, *Gondwana Res.* **7**, 1, 91–101. https://doi.org/10.1016/S1342-937X(05)70308-7.

Horibe Y., Craig H. (1995) D/H fractionation in the system methane-hydrogen-water, *Geoch. Cosm. Acta* **59**, 24, 5209–5217. https://doi.org/10.1016/0016-7037(95)00391-6.

Horsfield B., Mahlstedt N., Weniger P., Misch D., Vranjes Wessely S., Han S., Wang C. (2022) Molecular hydrogen from organic sources in the deep Songliao Basin, PR China, *Int. J. Hydrog. Energy* **47**, 38, 16750–16774. https://doi.org/10.1016/j.ijhydene.2022.02.208.

Johnson A., Cheeseman S., Ferris J. (1999) Improved compilation of Antarctic Peninsula magnetic data by new interactive grid suturing and blending methods, *Ann. Geofisica* **42**, 2, 249–259. https://doi.org/10.4401/ag-3717.

Klein F., Bach W., McCollom T.M. (2013) Compositional controls on hydrogen generation during serpentinization of ultramafic rocks, *Lithos* **178**, 55–69. https://doi.org/10.1016/j.lithos.2013.03.008.

Klein F., Tarnas J. D., Bach W. (2020) Abiotic sources of molecular hydrogen on Earth, *Elements* **16**, 19–24. https://doi.org/10.2138/gselements.16.1.19.

Larin N., Zgonnik V., Rodina S., Deville E., Prinzhofer A., Larin V. N. (2015) Natural molecular hydrogen seepage associated with surficial, rounded depressions on the European Craton in Russia, *Nat. Resour. Res.* **24**, 369–383. https://doi.org/10.1007/s11053-014-9257-5.

Lefeuvre N., Truche L., Donzé F.-V., Gal F., Tremosa J., Fakoury R.-A., Calassou S., Gaucher E.C. (2022) Natural hydrogen migration along thrust faults in foothill basins: the North Pyrenean Frontal Thrust case study, *Appl. Geochem.* **145**, 105396. https://doi.org/10.1016/j.apgeochem.2022.105396.

Leila M., Loiseau K., Moretti I. (2022) Controls on generation and accumulation of blended gases ($CH_4/H_2/He$) in the Neoproterozoic Amadeus Basin, *Australia. Mar. Petrol. Geol.* **140**, 105643. https://doi.org/10.1016/j.marpetgeo.2022. 105643.

Lévy D., Roche V., Pasquet G., Combaudon V., Geymond U., Loiseau K., Moretti I. (2023) Natural H2 exploration: tools and workflows to characterize a play, *Sci. Tech. Energ. Transition* **78**, 27. https://doi.org/10.2516/stet/2023021.

Maiga O., Deville E., Laval J., Prinzhofer A., Diallo A.B. (2023a) Characterization of the spontaneously recharging natural hydrogen reservoirs of Bourakebougou in Mali, *Sci. Rep.* **13**, 1, 11876. https://doi.org/10.1038/s41598-023-38977-y.

Maiga O., Deville E., Laval J., Prinzhofer A., Diallo A.B. (2023b) Trapping processes of large volumes of natural hydrogen in the subsurface: The emblematic case of the Bourakebougou H_2 field in Mali, *Int. J. Hydrog. Energy* **50**, 640–647. https://doi.org/10.1016/j.ijhydene.2023.10.131.

Martins-Neto M.A. (2009) Sequence stratigraphic framework of Proterozoic successions in eastern Brazil, *Mar. Petrol. Geol.* **26**, 163–176. https://doi.org/10.1016/j.marpetgeo.2007. 10.001.

Moretti I., Prinzhofer A., Françolin J., Pacheco C., Rosanne M., Rupin F., Mertens J. (2021a) Long term monitoring of natural hydrogen superficial emissions in a Brazilian cratonic environment. Sporadic large pulses versus daily periodic emissions, *Int. J. Hydrog. Energy.* **46**, 5, 3615–3628. https://doi.org/10.1016/j.ijhydene.2020.11.026.

Moretti I., Brouilly E., Loiseau K., Prinzhofer A., Deville E. (2021b) Hydrogen emanations in intracratonic areas: new guide lines for early exploration basin screening, *Geosciences* **11**, 145. https://doi.org/10.3390/geosciences11030145.

Moretti I., Geymond U., Pasquet G., Aimar L., Rabaute A. (2022) Natural hydrogen emanations in Namibia: field acquisition and satellite image analysis, *Int. J. Hydrog. Energy* **47**, 84, 3588–35607. https://doi.org/10.1016/j.ijhydene.2022.08.135.

Moretti I., Bouton N, Ammouial J., Carrillo A. (2024) The H_2 potential of the Colombian coals in natural conditions, *Int. J. Hydrog. Energy* **77**, 1443–1456. https://doi.org/10.1016/j.ijhydene.2024.06.225.

Myagkiy A., Brunet F., Popov C., Krüger R., Guimarães H., Charlet L., Moretti I. (2019) H_2 dynamics in the soil of an H_2-emitting zone (São Francisco Basin, Brazil): Microbial uptake quantification and reactive transport modelling, *Appl. Geochem.* **112**, 104474. https://doi.org/10.1016/j.apgeochem.2019.104474.

Myagkiy A., Moretti I., Brunet F. (2020) Space and time distribution of subsurface H_2 concentration in so-called "fairy circles": insight from a conceptual 2-D transport model, *Bull. Soc. Géol. Fr* **191**, 13. https://doi.org/10.1051/bsgf/2020010.

Pasquet G., Houssein Hassan R., Sissmann O., Varet J., Moretti I. (2022) An attempt to study natural H_2 resources across an oceanic ridge penetrating a continent: The Asal–Ghoubbet Rift (Republic of Djibouti), *Geosciences* **12**, 16. https://doi.org/10.3390/geosciences12010016.

Prinzhofer A., Pernaton E. (1997) Isotopically light methane in natural gases: bacterial imprint or segregative migration? *Chem. Geol.* **42**, 193–200. https://doi.org/10.1016/S0009-2541(97)00082-X.

Prinzhofer A., Cissé C.S.T., Diallo A.B. (2018) Discovery of a large accumulation of natural hydrogen in Bourakebougou (Mali), *Int. J. Hydrog. Energy* **43**, 19315–19326. https://doi.org/10.1016/j.ijhydene.2018.08.193.

Prinzhofer A., Moretti I., Françolin J., Pacheco C., D'Agostino A., Werly J., Rupin F. (2019) Natural hydrogen continuous emission from sedimentary basins: the example of a Brazilian H_2-emitting structure, *Int. J. Hydrog. Energy* **44**, 12, 5676–5685. https://doi.org/10.1016/j.ijhydene.2019.01.119.

Prinzhofer A, Cacas-Stentz M.C. (2023) Natural hydrogen and blend gas: a dynamic model of accumulation, *Int. J. Hydrog. Energy* **48**, 57, 21610–21623. https://doi.org/10.1016/j.ijhydene.2023.03.060.

Prinzhofer A, Rigollet C, Leufeuvre N., Françolin J., Miranda P. E. (2024) Maricá (Brazil), the new natural hydrogen play which changes the paradigm of hydrogen exploration, *Int. J. Hydrog. Energy* **62**, 91–98. https://doi.org/10.1016/j.ijhydene.2024.02.263.

Reis H.L.S., Alkmim F.F. (2015) Anatomy of a basin-controlled foreland fold-thrust belt curve: the Três Marias salient, São Francisco basin, Brazil, *Mar. Petrol. Geol.* **66**, 4, 711–731. https://doi.org/10.1016/j.marpetgeo.2015.07.013.

Reis H.L.S., Fonseca R.C.S. (2021) Does the unusual geochemical composition of the São Francisco basin natural gas (E Brazil) reveal typical characteristics of ancient and overmature petroleum systems?, in: *Goldschmidt 2021*, Virtual, 4–9 July. https://doi.org/10.7185/gold2021.6383.

Reis H.L.S., Suss J.F., Fonseca R.C.S., Alkmim F.F. (2017) Ediacaran forebulge grabens of the southern São Francisco basin, SE Brazil: Craton interior dynamics during West Gondwana assembly, *Precambrian Res.* **302**, 150–170. https://doi.org/10.1016/j.precamres.2017.09.023.

Reis H.L.S. (2018) *Gás natural*, Recursos Minerais de Minas Gerais (CODEMGE), Belo Horizonte, Available at http://recursomineralmg.codemge.com.br/substancias-minerais/gas-natural/#ANP2018.

Roche V., Geymond U., Boka-Mene M., Delcourt N., Portier E., Moretti I. (2024) The Damara Belt in Namibia: a new continental hydrogen play, *Sci. Rep.* **14**, 11655. https://doi.org/10.1038/s41598-024-62538-6.

Sgarbi P.B.A., Valenca J. G. (1995) Mineral and rock chemistry of Mata da Corda Kamafugitic Rocks (Minas Gerais State, Brazil), *An. Acad. Bras. Ciênc.* **57**, 2, 257–270.

Teixeira W., Oliveira E.P., Marques L.S. (2017) Nature and evolution of the Archean Crust of the São Francisco Craton, in: Heilbron M., Cordani U., Alkmim F. (eds), *São Francisco Craton, Eastern Brazil. Regional geology reviews*, Springer, Cham, pp. 29–56. https://doi.org/10.1007/978-3-319-01715-0_3.

Tribaldos V.R., White N.J., Roberts G. G., Hoggard M.J. (2017) Spatial and temporal uplift history of South America from calibrated drainage analysis, *Geochem. Geophys. Geosyst.* **18**, 6, 2321–2353. https://doi.org/10.1002/2017GC006909.

Truche L., Joubert G., Dargent M., Martz P., Cathelineau M., Rigaudier T., Quirt D. (2018) Clay minerals trap hydrogen in the Earth's crust: Evidence from the Cigar Lake uranium deposit, Athabasca, *Earth Planet. Sci. Lett.* **493**, 186–197. https://doi.org/10.1016/j.epsl.2018.04.038.

Vale Annual Report (2023) *Formulário de Relatório anual 20-F*, VALE S.A., Rio de Janeiro. Available at https://ri-vale.mz-sites.com/en/information-to-the-market/annual-reports/20-f-form/.

Zalán P.V., Silva P.C.R. (2007) Bacia de São Francisco, *Bol. Geociencias Petrobras* **15**, 2, 561–571.

Zgonnik V. (2020) The occurrence and geoscience of natural hydrogen: a comprehensive review, *Earth Sci. Rev.* **203**, 103140. https://doi.org/10.1016/j.earscirev.2020.103140.

Zgonnik V., Beaumont V., Deville E., Larin N., Pillot D., Farrell K. (2015) Evidence for natural molecular hydrogen seepage associated with Carolina bays (surficial, ovoid depressions on the Atlantic Coastal Plain, Province of the USA), *Earth Planet. Sci. Lett.* **2**, 31. https://doi.org/10.1186/s40645-015-0062-5.

Appendix

Description of methods

A significant amount of exploratory data of the São Francisco Basin, including seismic surveys, wells data, and geochemical studies are public domain, available by the Brazilian National Agency of Petroleum, Natural Gas and Biofuels (ANP) in cooperation with the Geological Survey of Brazil (SGB). Additionally, high-resolution aeromagnetic data are available for free consultation and download in the database of the Geological Survey of Brazil (GSB, https://www.geosgb.cprm.gov.br).

A.1. Satellite images

Satellite images were useful for identifying SCDs in the whole study area. It used Google and Esri satellite images were provided by the Quick Map Services plug-in of the software QGIS.

The position and characteristics, such as shape and density, of SCD were contrasted to the main structural and geological framework, and well locations, in order to recognize links and patterns between features.

In addition, the location of those features has been used as a baseline for the search for features indicative of fluid flux in seismic interpretation.

A.2. Geophysical surveys

The geophysical studies were based on 14 2D time-migrated seismic surveys and the compilation of the high-resolution aeromagnetic survey (Correa, 2019), as well as the magnetic maps presented on the Brazilian Geological Survey website (https://geoportal.sgb.gov.br/geosgb), which include airborne magnetic surveys (1000, 2000, 3000, and 4000 series) and a magnetic anomaly map.

The available seismic lines were used to interpret the top of the basement horizon in the entire study area using Petrel version 2020.5. None of the wells were drilled to the basement, however, their lithostratigraphic markers offer a guideline for the basement interpretation. Compared to superimposed layers, the basement presents a dissimilar seismic character, such as chaotic reflectors and middle to low acoustic impedance. Locally, especially around the wells and using the top markers, it was interpreted the Sete Lagoas Formation and Macaúbas and Paranoá Sequences horizons. Extended faults and major decoupled layers were also mapped.

Based on these data it was mapped the possible locals of occurrence of Archean/Paleoproterozoic basement, considered a probable H_2 source rock, and recognized the important structures that connect the basement to the H_2 occurrences (wells and seeps).

The low thickness, up to 20 m, of the H_2-rich layers identified in the wells is incompatible to the seismic scale resolution. Thereby, the recognition of the seismic response of these layers was not possible.

Since the presence of iron-rich rocks in the subsurface is associated with magnetic anomalies, magnetic data are a powerful tool to infer the location of source rocks for H_2 and large structures underground.

The Total Field Anomaly of the study area (detailed in Sect. 3, Fig. 7) was extracted from the Magnetic Anomaly Map of Brazil (Correa, 2019). According to the author, the magnetic data was interpolated in a regular grid (0.0101 x 0.0101 degree) using the suture method (Johnson *et al.*, 1999) to integrate the projects with a flight height of 1000 m. To minimize the differences between the various IGRF (International Geomagnetic Reference Field) models used, Correa (2019) suppressed wavelengths greater than 330 km through a Gaussian high-pass filter and replaced by the lithospheric magnetic model MF 7 (Hemant *et al.*, 2007; Maus *et al.*, 2008).

The magnetic data were processed using the software Geosoft Oasis montaj©, Version 9.9, 2020. Over the Total Field Anomaly (TFA) information, we applied several enhancement methods of magnetic anomalies: First Vertical Derivative (VDR1, Evjen, 1936); Second Vertical Derivative (VDR2, Peters, 1949; Elkins, 1951); Analytic Signal Amplitude (ASA, Nabighian, 1972; Roest *et al.*, 1992); Total Horizontal Derivative (THDR, Cordell and Grauch, 1982, 1985); Tilt Derivative (Miller and Singh, 1994); Vertical Integral (VI, Silva, 1996); Analytic Signal of the Vertical Integral (ASVI, Paine *et al.*, 2001); Vertical Integral of the Analytic Signal (VIAS, Paine *et al.*, 2001); Total Horizontal Derivative of the Tilt Derivative (Verduzco *et al.*, 2004), as well a combination of techniques such as: Improved Analytic Signal of the Vertical Integral (IASA, Ma and Du, 2012); Tilt Angle of

the Horizontal Gradient (TAHG, Ferreira *et al.*, 2013; First Vertical Derivative of the Total Horizontal Derivate of the Tilt Derivative (VDR1-THDR-TDR, Zhang *et al.*, 2015); Enhanced Tilt Angle of the Horizontal Gradient (THGED, Pham et al., 2023).

The depth of the most evident magnetic anomaly of the study area, Pirapora Anomaly, was estimated using the 3D Euler deconvolution (Thompson, 1982; Reid *et al.*, 1990), a tool for semi-quantitative interpretation. This method calculates the estimated depth of the sources based on window size and a specific structural index (SI) for each type of geologic feature. For the Pirapora Anomaly it was adopted SI = 2, corresponding to a cylinder/pipe model. The Euler deconvolution is expressed using the following equation:

$$(x - x_0)\frac{\delta M}{\delta x} + (y - y_0)\frac{\delta M}{\delta y} + (z - z_0)\frac{\delta M}{\delta z} = N(B - M).$$

Assuming that B is the regional magnetic field (longer wavelengths); N is the degree of homogeneity given by SI; M is the potential field observation at the point (x, y, z), and (x_0, y_0, z_0) are the coordinates of a point on the source.

The 3D Euler deconvolution was applied in the TFA and VIAS grid to depth estimates. The maximum depth percentage of error was 2% and the window size was equal to 2500 m.

The results of the original formulation of Euler deconvolution (Reid *et al.*, 1990; Thompson, 1982), present some limitations, such as a large number of spurious solutions and the difficulty of choosing the correct structural index (SI). The SI is linked to the type of geological source and represents the fall-off of field strength versus distance from the source. To reduce the number of solutions, we used the criterion (depth tolerance = 2%) suggested by Thompson (1982). Considering the shape of the Pirapora anomaly, the structural index (SI = 2, cylinder/pipe model) is the most appropriate.

Several methods have been proposed that aim to minimize the aforementioned limitations of Euler deconvolution (Barbosa *et al.*, 1999; Castro *et al.*, 2020; FitzGerald *et al.*, 2004; Florio *et al.*, 2006; Hansen and Suciu, 2002; Keating and Pilkington, 2004; Melo *et al.*, 2013; Melo and Barbosa, 2020); Mikhailov *et al.*, 2003; Mushayandebvu *et al.*, 2001, 2003; Nabighian and Hansen, 2001; Ravat, 1996; Reid *et al.*, 2014; Salem and Ravat, 2003; Silva and Barbosa, 2003; Ugalde and Morris, 2010; Williams *et al.*, 2005).

A.3. Geochemistry

The available 334 gas geochemical data from 15 wells underwent quality control, first checking the reliability of the data, since we did not perform the analyses. In total, 334 gas composition analyses are collected from different depths, using three different types of sampling containers: cylinder (15 samples), isotube (136 samples), and isojar (175 samples). Also, there are available eight samples with no container indication, probably corresponding to isotube or isojar. No information was provided on the method of sampling, we assume that all gas samples were collected in the wellhead, using the different containers already mentioned.

The cylinder samples were collected during the well tests and their analyses show good reliability, as they present very consistent results and information about the parameters used. The isotube and isojar gas analyses are numerous, but their dataset is very dubious, and control process and laboratory reports are absent. Particularly, the headspace method used in isojar is not efficient

in preserving the original composition of gas in the subsurface, especially H_2 due to its volatile character. Additionally, even for the same well and depth, in some cases, isotube and isojar data are very conflicting between them, also when compared to cylinder data.

In addition, in the database there are two groups of gas compositional analysis results a) in ppm, which do not present He measurements and include all isotube and isojar, and four cylinders samples; and b) in %vol, with He values, encompassing most of the cylinder samples. The first group appears to have a high detection limit for H_2 as they show only values higher than 12,500 ppm (1.2%), even when cylinder analysis indicated 0.07% of H_2 for the same depth.

The other potential issue associated with gas sampled while drilling (isotube and isojar) is the possible DBT (Drill Bit Metamorphism): H_2 may be artificially generated during the drilling, through mechanical cracking of water and HC molecules. This problem disappears when using test samples, such as cylinder samples, as this transient artifact is gone.

In summary, the quantitative gas characterization was focused on the 15 cylinder samples from only 4 wells. This dataset went through a modern air contamination correction, using the O_2 content of the sample and the air current N_2/O_2 ratio, to recalculate the amount of N_2 and then normalize all gas values to 100%. One of the samples from well PTRA-1 was eliminated due to the high content of air contamination, and also due to the leakage indication in the analysis reports. Therefore, our dataset for geochemical assessment was concentrated in 14 samples with compositional and isotopic analysis (Table 1). The wells PTRA-6, PTRA-10, PTRA-12, and PTRA-13 have not been considered for the geochemical evaluation since the data was of too bad quality, but they are defined as H_2 host wells.

It should be highlighted that the name of the wells 1-PTRA-1-MG, 1-PTRA-2-MG, 1-PTRA-5-MG, 1-PTRA-6-MG, 1-PTRA-10-MG, 1-PTRA-12-MG, and 1-PTRA-13-MG were simplified respectively to PTRA-1, PTRA-2, PTRA-5, PTRA-6, PTRA-10, PTRA-12, PTRA-13 and PTRA-14, for easy reading.

References of Appendix

Barbosa V.C.F., Silva J.B.C., Medeiros W.E. (1999) Stability analysis and improvement of structural index estimation in Euler deconvolution, *Geophysics* 64, 1, 48–60. https://doi.org/10.1190/1.1444529.

Castro F.R., Oliveira S.P., de Souza J., Ferreira F.J.F. 2020. Constraining Euler deconvolution solutions through combined tilt derivative filters. *Pure Appl. Geophys.* 177, 4883–4895. https://doi.org/10.1007/s00024-020-02533-w.

Correa R.T. (2019) Magnetic anomaly map of Brazil (third edition). Scale 1:5,000,000. Geological Survey of Brazil (SGB). Available at https://geosgb.sgb.gov.br/geosgb/downloads_en.html.

Cordell L., Grauch V.J.S. (1982) Mapping basement magnetization zones from aeromagnetic data in the San Juan Basin, New Mexico, in: *SEG Technical Program Expanded Abstracts*, Society of Exploration Geophysicists, pp. 246–247. https://doi.org/10.1190/1.1826915.

Cordell L., Grauch V.J.S. (1985) Mapping basement magnetization zones from aeromagnetic data in the San Juan Basin, New Mexico, in: Hinze W.J. (ed), *The utility of regional gravity and magnetic anomaly maps,* Society of Exploration Geophysicists, pp. 181–197. https://doi.org/10.1190/1.0931830346.ch16.

Elkins T.A. (1951) The second derivative methods of gravity interpretation, *Geophysics* 16, 29–50. https://doi.org/10.1190/1.1437648.

Evjen H.M. (1936) The place of the vertical gradient in gravitational interpretations, *Geophysics* 1, 127–136. https://doi.org/10.1190/1.1437067.

Ferreira F.J.F., Souza J., Bongiolo A.B.S., Castro, L.C. (2013) Enhancement of the total horizontal gradient of magnetic anomalies using the tilt angle, *Geophysics* 78, J33–J41. https://doi.org/10.1190/geo2011-0441.1.

FitzGerald D., Reid A., McInerney P. (2004). New discrimination techniques for Euler deconvolution. *Comput. Geosci.* 30, 5, 461–469. https://doi.org/10.1016/j.cageo.2004.03.006.

Florio G., Fedi M., Pasteka R. (2006). On the application of Euler deconvolution to the analytic signal. *Geophysics* 71, 6, L87–L93. https://doi.org/10.1190/1.2360204.

Hansen R.O., Suciu L. (2002) Multiple-source Euler deconvolution, *Geophysics* 67, 525–535. https://doi.org/10.1190/1.1468613.

Hemant K., Thébault E., Mandea M., Ravat D., Maus S. (2007) Magnetic anomaly map of the world: merging satellite, airborne, marine and ground-based magnetic data sets, *Earth Planet. Sci. Lett.,* 260, 56–71. https://doi.org/10.1016/j.epsl.2007.05.040.

Keating P., Pilkington M. (2004). Euler deconvolution of the analytic signal and its application to magnetic interpretation, *Geophys. Prospect.* 52, 3, 165–182. https://doi.org/10.1111/j.1365-2478.2004.00408.x.

Ma G., Du X. (2012) An improved analytic signal technique for the depth and structural index from 2D magnetic anomaly data, *Pure Appl. Geophys.* 169, 2193–2200. https://doi.org/10.1007/s00024-012-0484-6.

Maus S., Yin F., Luhr H., Manoj C., Rother M., Rauberg J., Michaelis I., Stolle C., Muller R. D. (2008) Resolution of direction of oceanic magnetic lineations by the sixth-generation lithospheric magnetic field model from CHAMP satellite magnetic measurements, *Geochem. Geophys. Geosyst.* 9, 7, 1–10. https://doi.org/10.1029/2008GC001949.

Melo F. F., Barbosa V. C. F. (2020) Reliable Euler deconvolution estimates throughout the vertical derivatives of the total-field anomaly, *Comput. Geosci.* 138, 104436. https://doi.org/10.1016/j.cageo.2020.104436.

Melo F. F., Barbosa V. C. F., Uieda L., Oliveira V. C., Jr., Silva J. B. C. (2013) Estimating the nature and the horizontal and vertical positions of 3D magnetic sources using Euler deconvolution, *Geophysics*, 78, 6, J87–J98. https://doi.org/10.1190/geo2012-0515.1.

Mikhailov V., Galdeano A., Diament M., Gvishiani A., Agayan S., Boboutdinov S., Graeva E., Sailhac P. (2003) Application of artificial intelligence for Euler solutions clustering, *Geophysics* 68, 168–180. https://doi.org/10.1190/1.1543204.

Miller H.G., Singh V. (1994) Potential field tilt a new concept for location of potential field sources. *J. Appl. Geophys.*, 32, 213–217. https://doi.org/10.1016/0926-9851(94)90022-1.

Mushayandebvu M.F., van Driel P., Reid A.B., Fairhead J.D. (2001) Magnetic source parameters of two-dimensional structures using extended Euler deconvolution, *Geophysics* 66, 814–823. https://doi.org/10.1190/1.1444971.

Mushayandebvu M.F., Lesur V., Reid A.B., Fairhead J.D. (2003) Grid Euler deconvolution with constraints for twodimensional structures, *Geophysics* 69, 489–496. https://doi.org/10.1190/1.1707069.

Nabighian M.N. (1972) The analytic signal of two-dimensional magnetic bodies with polygonal cross-section: its properties and use for automated anomaly interpretation, *Geophysics* 37, 507–517. https://doi.org/10.1190/1.1440276.

Nabighian M.N., Hansen R.O. (2001) Unification of Euler and Werner deconvolution in three dimensions via the generalised Hilbert transform, *Geophysics* 66, 1805–1810. https://doi.org/10.1190/1.1487122.

Paine J., Haederle M., Flis M. (2001) Using transformed TMI data to invert for remanently magnetised bodies, *Exploration Geophysics,* 32, 3–4, 238–242. https://doi.org/10.1071/EG01238.

Peters L.J. (1949) The direct approach to magnetic interpretation and its practical application, *Geophysics* 14, 290–320. https://doi.org/10.1190/1.1437537.

Pham L.T., Van Duong H., Kleu Duy T., Oliveira S. P., Lai G. M., Bul T. M., Oksum E. (2023) An effective edge detection technique for subsurface structural mapping from potential field data, *Acta Geophys.* 72, 1661–16744. https://doi.org/10.1007/s11600-023-01185-3.

Ravat D. (1996) Analysis of the Euler method and its applicability in environmental magnetic investigations. Journal of Environmental and Engineering, *Geophysics* 1, 229–238. https://doi.org/10.4133/jeeg1.3.229.

Reid A.B., Allsop J.M., Granser H., Millett A., Somerton I.W. (1990) Magnetic interpretation in three dimensions using Euler deconvolution, *Geophysics* 55, 80–91. https://doi.org/10.1190/1.1442774.

Reid A. B., Ebbing J., Webb S. J. (2014) Avoidable Euler Errors – the use and abuse of Euler deconvolution applied to potential fields, *Geophys. Prospect.* 62, 5, 1162–1168. https://doi.org/10.1111/1365-2478.12119.

Roest W. R. J., Verhoef J., Pilkington M. (1992) Magnetic interpretation using the 3-D Analytic signal, *Geophysics*, 57, 116–125. https://doi.org/10.1190/1.1443174.

Salem A., Ravat D. (2003) A combined analytic signal and Euler method (AN-EUL) for automatic interpretation of magnetic data. *Geophysics* 68, 6, 1952–1961. https://doi.org/10.1190/1.1635049.

Silva J.B.C. (1996) 2-D magnetic interpretation using the vertical integral, *Geophysics* 61, 2, 387–393. https://doi.org/10.1190/1.1443967.

Silva J. B. C., Barbosa V. C. F. (2003) 3D Euler deconvolution: theoretical basis for automatically selecting good solutions, Geophysics, 68, 6, 1962–1968. https://doi.org/10.1190/1.1635050.

Thompson D.T. (1982) EULDPH: a new technique for making computer-assisted depth estimates from magnetic data, *Geophysics* 47, 31–37. https://doi.org/10.1190/1.1441278.

Ugalde H., Morris W.A. (2010) Cluster analysis of Euler deconvolution solutions: new filtering techniques and geologic strike determination, *Geophysics* 75, 3, L61–L70. https://doi.org/10.1190/1.3429997.

Verduzco B., Fairhead J.D., Green C.M., MacKenzie C. (2004) New Insights into Magnetic Derivatives for Structural Mapping. *Lead. Edge* 23, 116–119. https://doi.org/10.1190/1.1651454.

Williams S.E., Fairhead J.D., Flanagan G. (2005) Comparison of grid Euler deconvolution with and without 2D constraints using a realistic 3D magnetic basement model, *Geophysics* 70, 3, L13–L21. https://doi.org/10.1190/1.1925745.

Zhang X., Yu P., Tang R., Xiang Y., Zhao C. (2015) Edge enhancement of potential field data using an enhanced tilt angle, *Explor. Geophys.* 46, 3, 276–283. https://doi.org/10.1071/EG13104.